# Assessment of Defects in Steel Structures Using UAVs and Image-Based 3D Reconstruction

BY:

NALIN NARANJO

B.S., University of Illinois at Chicago, 2020

THESIS

Submitted as partial fulfillment of the requirements

for the degree of Master of Science in Civil Engineering

in the Graduate College of the

University of Illinois at Chicago, 2021

Chicago, Illinois

Defense Committee:

Dr. Didem Ozevin, Chair and Advisor

Dr. Lesley Sneed, Civil, Materials, and Environmental Engineering

Dr. Farid Peiravian, Civil Materials, and Environmental Engineering

This thesis is dedicated to my parents, Natakan Naranjo and Edinson Albeiro Naranjo. Thank you for believing in me.

**ACKNOWLEDGEMENTS**

I would like to thank my thesis committee, Dr. Didem Ozevin, Dr. Lesley Sneed, and Dr. Farid Peiravian for their time, support, and willingness to review this thesis. I also wish to thank the many people who have supported me along the production of my thesis. First and foremost, I would like to extend my deepest gratitude to Dr. Didem Ozevin for her invaluable advice, continuous encouragement, and unwavering guidance as well as the opportunity to undertake research on this topic. She helped me gain more confidence in my abilities and the skills I have learned from conducting this research have opened many new doors in my life. I would also like to thank her for her patience, support and understanding while I adjusted to working in the industry. Many thanks to Eric Schmidt and Joel Rodriguez for their help in determining feasible methods to manufacture the parts needed for my experiment. I would like to give a special thanks to Dylan Lynch for his quick responses to my emails and for quickly manufacturing the parts I needed, which helped my experiments get completed faster. Much appreciation to Junaid Ahmed and Dr. Matthew Daly for their time and assistance during tensile testing. Thank you to Gorkem Okudan for his assistance and guidance during numerical modelling. Thank you to Tonghao Zhang for his help with enhancing the optical microscope video and for his support. Much appreciation to Jennifer Vetrone for her advice in both research and industry. Special thanks to Tanja Rakovic for her feedback, assistance, and encouragement during the production of this thesis.

## TABLE OF CONTENTS

CHAPTER PAGE

## LIST OF TABLES

TABLE PAGE

## LIST OF FIGURES

FIGURE PAGE

## LIST OF ABBREVIATIONS

| | |
|---|---|
| UAV | Unmanned Aerial Vehicle |
| AASHTO | American Association of State Highway and Transportation Officials |
| FOV | Field of View |
| FHWA | Federal Highway Administration |
| NDE | Nondestructive Evaluation |
| ASTM | American Society for Testing and Materials |
| SHM | Structural Health Monitoring |
| IR | Infrared |
| GPS | Global Positioning System |
| TLS | Terrestrial Laser Scanning |
| CRP | Close Range Photogrammetry |
| IS | Infrared Scanning |
| BrIM | Bridge Information Modelling |
| SfM | Structure from Motion |
| DJI | Da-Jiang Innovations |
| FEM | Finite Element Method |

## SUMMARY

The primary goal of this thesis is to develop a methodology for which one could generate a 3D reconstructed model from Unmanned Aerial Vehicle (UAV) captured images that has high enough quality for bridge inspection. The 3D models in this thesis were evaluated qualitatively and quantitatively. The models evaluated include ad hoc trials and a trial using the methodology. This thesis also evaluates the utility of 2D images from the DJI Phantom 4 Pro UAV's camera for the qualitative and quantitative measurement of defects. Finally, a passive visual sensor was developed to make it possible for non-visual plastic deformations to be indirectly measured visually.

For 3D reconstruction and image processing objectives, experimental studies were conducted on a 2.58 m long girder with dimensions similar to a HP8x36 using the DJI Phantom 4 Pro UAV. Calibration sheets were attached to the girder for unit conversions between arbitrary 3D model units and real-world units as well as for 2D image processing for defect measurements. The girder was positioned on the ground for the experiments, elevated by a dolly. For developing a passive visual sensor, both numerical and experimental studies were conducted. The numerical study was done using ANSYS Static Structural to simulate a tensile test using a steel coupon with the preliminary sensor designs attached. From the model, the time between the coupon's yield stress and the sensor's ultimate stress were used to determine the best sensor geometry and materials. During the experimental trial, the tensile test was conducted using a model 1125 MTS tensile machine with a load rate of 2 mm/min on the coupon and sensor setup bonded using Loctite® E-120hp adhesive.

It was found that the best practices for reconstructing the 3D model are to use many camera angles and elevations and to take images close to the structure. It was also important that whatever that would be used as a marker in the model for scale should have enough

photos devoted to it to ensure that it does not get distorted and impact the quantitative accuracy of the model. Image processing results showed that light helped improve the quality of images and that 90 mm lengths could be measured with high accuracy but that 2 mm lengths could not achieve the same accuracy levels. The passive sensor experimental tests showed that more work is needed to improve the bond between the sensor and the coupon since the adhesive failed prematurely.

Future works include testing the proposed methodology on a more realistic setup such as the girder positioned on the ceiling and more confinement, testing the methodology on larger girder sizes, and using a UAV suitable for bridge inspection. For 2D image processing, limits on defect sizes that can be captured by the DJI Phantom 4 Pro with satisfactory accuracy could be studied and different image processing masks could be tested with more realistic defects rather than a calibration sheet. Lighting methods could be developed to illuminate the underside of bridges for better UAV image quality in realistic situations. For the passive sensor, better attachment methods or new designs should be developed.

# 1. INTRODUCTION

## 1.1 Problem Statement

Traditional bridge inspection practices typically require bridges and roadways to be closed down so equipment can be set up to bring the inspector close enough to perform their job. This is a time consuming, disruptive, and expensive process. Additionally, the need to bring the inspector up to the bridge adds a safety risk to this process and the subjectivity of damage quantification in inspections adds to inconsistency. Unmanned Aerial Vehicles (UAVs) are less disruptive to traffic, keep inspectors safe, and can provide new perspectives to digital life cycle monitoring of structures. They can be used to collect data for image-based 3D reconstruction which results in a 3D model that can be accessed in house by inspectors, reducing the disruption to traffic and increasing safety and convenience. But, for inspectors to be able to conduct inspections using a 3D model, the model needs to be highly accurate in both geometry and texture.

The complex geometry of steel sections such as W-shapes requires effective path planning to fully reconstruct 3D geometry with the best resolution possible. For example calculations in this thesis, a resolution of 2 mm was chosen considering the physical limitations of existing UAVs. This value was chosen since there was no quantitative defect size listed in the AASHTO Bridge Element Inspection Manual. Condition state definitions for cracking in steel members is based on whether a crack exists and, if it does, whether it is arrested [1]. This value can be any value that best fits the goals of the situation at hand. Chen S. et al. showed that the image resolution depends on the working distance and field of view (FOV) of the UAV camera [2]. The proposed framework in this thesis provides a systematic data collection approach for maximizing the outputs of UAV inspection for geometric details and eliminating missing data points that lead to inaccurate 3D reconstruction.

## 1.2 Objectives and Approach

The objective of this thesis is to determine and optimize the accuracy of defect and dimensional measurements from images captured by drone camera and through 3D reconstruction of images. This is accomplished by creating a methodology for using UAVs to capture images for the accurate 3D reconstruction of multi-girder steel bridges. In addition to being effective, the path proposed in the methodology needs to be simple to fly to make it easier for UAV pilots of varying skill level to adopt in addition to the enhanced time efficiency for reducing the power consumption. In this thesis, a passive and UAV-friendly sensor is also developed that would allow non-visual plastic deformations to be detected more easily via visual inspection. The sensor is made of a geometric configuration such that strain is amplified as compared to the base structure. The geometric configuration of the mechanical sensor can be tuned at the level that the sensor element would reach the rupture point when the base structure reaches yield strain. As such, the over-stress state of the base structure could be indirectly captured by UAV camera due to visual failure of the mechanical sensor elements. The sensors can be used to determine the extent of damage caused by bridge girder deformation.

There were different research approaches to reach each objective of this thesis. To create a data collection methodology for the accurate 3D reconstruction of multi-girder steel bridges trials using ad hoc data collection were conducted to understand and become familiar with the logistics of piloting a UAV and using 3D reconstruction software ContextCapture from Bentley. 3D reconstructed model data were observed and collected within ContextCapture. To test the accuracy of measurements in 2D images, a calibration sheet was created, and images were captured at varying distances. 2D image data was extracted using the Image Processing Toolbox from Mathworks.

For developing a passive sensor, numerical models were performed using the ANSYS Static Structural module to determine the appropriate dimensions and material for the sensor to

behave appropriately under the desired triggering condition. Experimental tests were performed as a proof of concept using coupons made of A572 Grade 50 steel with acrylic sensors attached using Loctite® E-120hp adhesive in a tensile test. Video was recorded via optical microscope of the tensile test to capture the behavior of the sensor as the coupon reached and surpassed the yield point for closer observation of the failure modes.

### 1.3 Structure of Thesis

The remainder of this work is structured as follows:

Section 2 provides background information on the problem, covering common types of bridge maintenance, damage, and current practices for bridge inspection. It continues with information on using UAVs for structural inspection and more specifically covers the topics of 3D reconstruction and image processing. Next, section 3 covers the topic of exploring and improving the accuracy of measurements able to be taken from 3D reconstructed models and 2D captured images. Following section 3, section 4 covers the topic of developing a passive sensor to increase the amount of information that a UAV can gather using a camera payload. Finally, section 5 summarizes the thesis, the major findings of this research, and provides suggestions for future works.

# 2. LITERATURE REVIEW

## 2.1 Introduction

UAVs can help make bridge inspections faster, safer, and less costly [3]. Using UAVs, inspectors can capture images from useful perspectives that may not be possible otherwise. Because of their maneuverability, UAVs can also be used to capture complete image sets for 3D reconstruction. 3D reconstructed models of bridges have potential to be used for structural inspectors to keep them safe and to allow for less time in the field. Currently, 3D reconstructed models of bridges do not have the resolution needed for inspectors to be able to rely on them for complete observations [4]. With improvements to 3D reconstruction image acquisition and methodology specifically for the reconstruction of bridges and bridge elements, 3D bridge models may be able to achieve the accuracy and resolution needed for inspections.

## 2.2 Bridge Maintenance

According to the Federal Highway Administration (FHWA) National Bridge Inspection Standards, bridges are mandated to be inspected at least once every 24 months. With special consent, bridges may be allowed to go 48 months before being inspected, but not more than that [5]. Depending on the condition of the bridge, inspections may be carried out more frequently [6], such as every year or twice a year. According to the American Association of State Highway and Transportation Officials (AASHTO) Manual for Condition Evaluation of Bridges, there are five different types of inspection that are performed on bridges [6]. Initial inspection is the first inspection of a bridge, and it is meant to provide a baseline for future observations. They may also be done after a change in the bridge such as a widening or lengthening. Routine inspections are the most common inspections. These are done as a regular checkup on bridge condition and functionality to see if there are any changes from previous records. In-depth inspections are for finding defects not readily found using routine inspections and are hands on. Damage inspections are done in the aftermath of damage

inflicted via the environment or human actions and special inspections are used to regularly monitor known or suspected structural defects.

### 2.2.1 Types of Bridge Defects

Bridges are subject to various types of defects. Defects in concrete include scaling, cracking, efflorescence, delamination, spalling, pop-outs, honeycombing, and leakages. Defects in sub-structure include settlement, scour, corrosion, cracking/fatigue, and connection failure. For this thesis, the focus is on superstructure defects on steel girders. These can be afflicted by corrosion, section loss, coating failures, fatigue cracks, local or global buckling, and elongation. At connections, there may also be broken or missing bolts. Examples of steel defects are shown in Figure 1 and Figure 2. With an accurate and precise 3D reconstructed model of a steel girder, detailed and quantifiable observations and measurements can be taken of these defects.

According to the FHWA Bridge Inspector's Reference Manual, corrosion occurs when the steel is exposed to wet and dry cycles and is accelerated when deicing chemicals are present [7]. Corrosion is the main reason for section loss in steel. Coating failures in steel members involve chalking, cracking, erosion, checking, and wrinkling. Corrosion related coating failures involve blistering, undercutting, pinpoint rusting, and mudcracking. Fatigue cracking is caused by repeated loading and can lead to sudden catastrophic bridge failure depending on the type of bridge. When overloaded or subject to collision steel members will plastically deform or completely fail. Overloads cause elongation and decrease in cross section in tension members. In compression members, overload can cause buckling in a single or double bow shape. Heat damage can also cause deformations in steel, but this only occurs in extreme heat at temperatures starting at approximately 316°C. These deformations are in the form of sagging which can cause members to undergo buckling or twisting. At the connection points, bolts and rivets will be prone to failure.

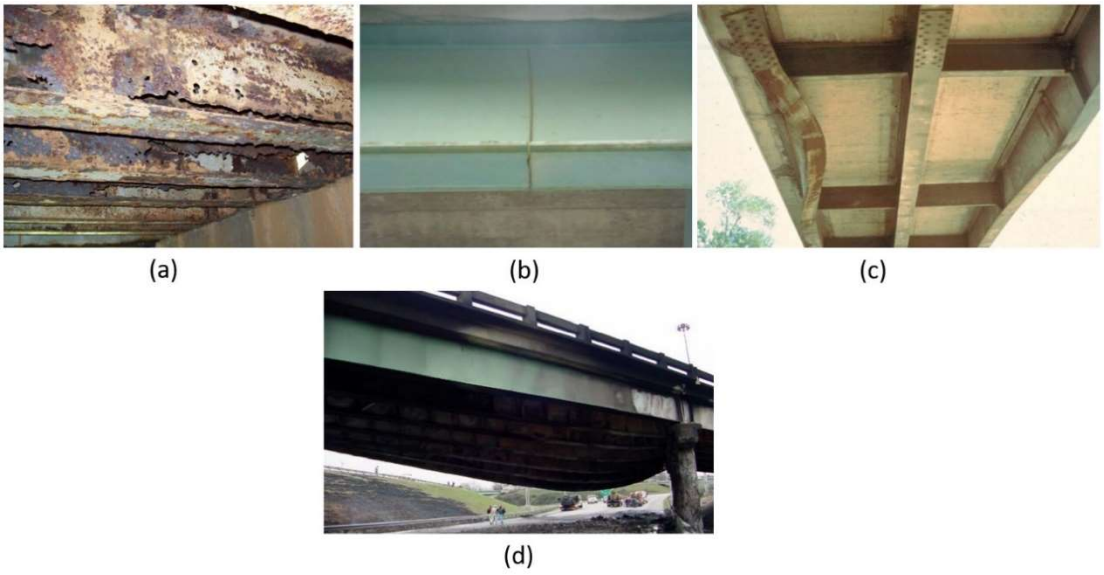


Figure 1. Examples of steel defects. (a) Corrosion and section loss, (b) Fatigue cracking, (c) Collision damage, (d) Heat damage [7].

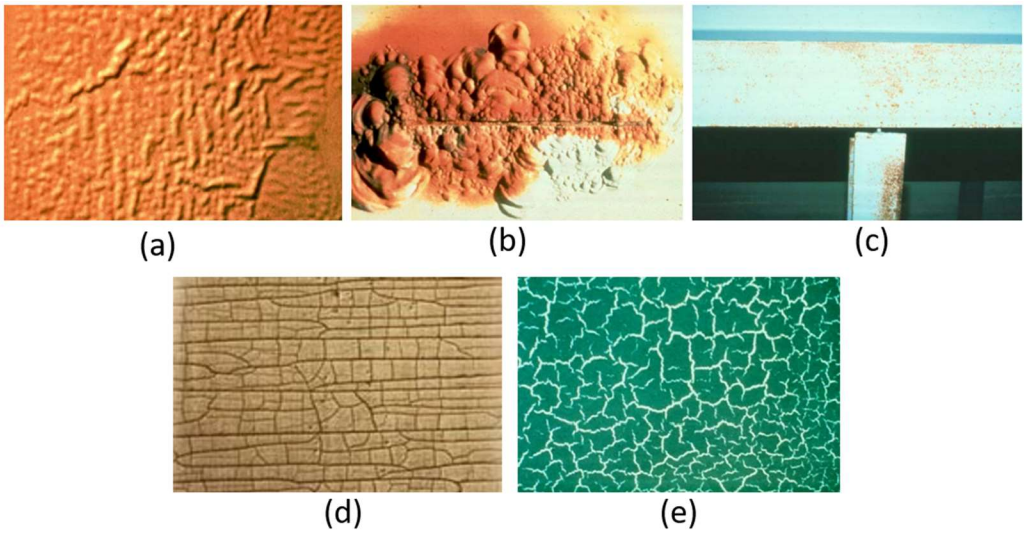


Figure 2. Examples of coating defects. (a) Wrinkling, (b) Rust undercutting at a scratched area, (c) Pinpoint rusting, (d) Paint peeling from steel bridge members, (c) Mudcracking paint [7].

### 2.2.2 Bridge Inspection Methods

According to the FHWA Bridge Inspector's Reference Manual, inspection methods used on steel bridge members involve visual inspection, physical methods, and advanced methods. A visual inspection is done first to identify problem areas [7]. Physical inspection involves removing paint and cleaning the surfaces to reveal damage. Removal of loose or flaked steel is also performed to determine severity of section loss and remains a limitation for UAVs. Advanced methods for steel inspection involve nondestructive and destructive methods. While UAVs cannot perform destructive testing, they have been able to perform some forms of nondestructive testing.

Nondestructive evaluation (NDE) methods are defined as methods to detect, locate, and measure flaws in materials that preserves a material's structural integrity [8]. There are various subcategories of NDE methods. The first subcategory is continuous versus periodic inspection. Continuous monitoring is also called structural health monitoring (SHM) and it involves continuous data collection using permanently attached sensors. Periodic inspection are inspections done based on a structure's age and deterioration. While UAVs cannot perform SHM, they are able to perform periodic inspection. The next subcategory is contact versus noncontact sensing and the final subcategory of NDE methods are quantitative versus qualitative sensing. As the name suggests, quantitative sensing can return information about the size, characteristics, and severity of defects while qualitative sensing returns visual information only. Common types of NDE methods are liquid penetrant, vibration, impact echo, ultrasonics, acoustic emission, visual image, thermography, and magnetic particle. Vibration, impact echo, ultrasonics, and acoustic emission are all quantitative methods. Liquid penetrant, visual image, thermography, and magnetic particle are qualitative methods. UAVs have been using visual image and thermographic methods with great success, but other methods have not been effectively applied as of yet. One exception is ultrasonics [9], which show promise for future use by UAVs.

Focusing in on NDE methods that are most commonly used by UAVs, infrared (IR) thermography has applications in the inspection of photovoltaic plants [10], wind turbines [11], and building inspection [12]. Relevant to bridge inspection, IR thermography can be used to detect moisture and water infiltration, but multiple images need to be captured over the course of approximately 24 hours for deep analysis [12]. For visual images, Kromanis and Forbes developed a low-cost robotic camera system for determining the structural response of a bridge [13].

According to the FHWA Bridge Inspector's Reference Manual, access to the underside of bridges can be granted using various methods [7]. Access to structures without the use of a vehicle involve techniques and equipment such as ladders, rigging, scaffolds, boats or barges, climbers, floats, rappelling, free climbing. The presence of permanent inspection structures may also be available. Types of access vehicles include a manlift, scissors lift, bucket truck, or an under bridge inspection vehicle. Figure 3 shows examples of some access methods. Using UAVs, inspectors can get a closer look without needing to risk themselves in this way.

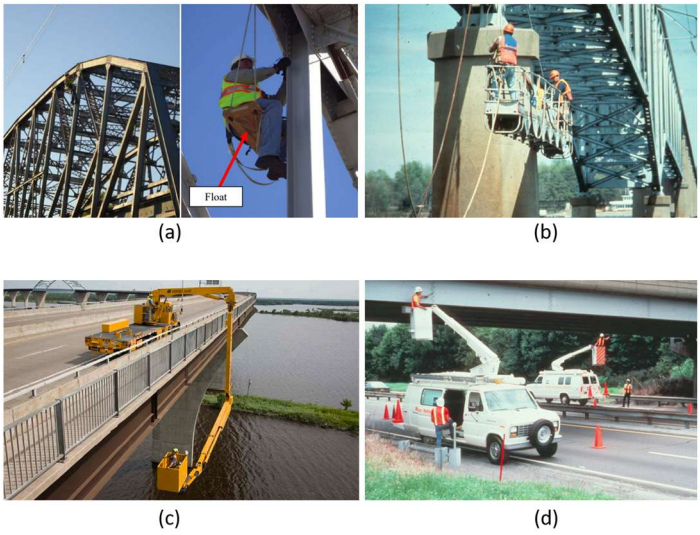


Figure 3. Examples of access methods. (a) Float, (b) Rigging, (c) Under bridge inspection vehicle, (d) Bucket truck [7].

Presently, UAVs are used as another tool for a bridge inspector's toolbox and not as a replacement for hands on inspection. UAVs can help avoid some of the many dangers inherent to bridge inspection as well as reduce inspection time by allowing for the optimization of the in-person inspection after a pre-inspection flight and to "relieve the inspector of having to take photos during the inspection" [3]. Photos are commonly taken during inspection for record keeping along with notes on plans to markup locations and descriptions of the defects found. Using a UAV to take images instead can help keep an inspector's hands free and allow for less multitasking in dangerous situations.

### 2.3 Structural Inspection using UAVs

There are 4 different subsets of UAVs: multi rotor, fixed wing, single rotor, and hybrid. Greenwood et al. describes the various types of UAVs [14]. Fixed wing and single rotor UAVs are suited for aerial mapping. Due to the fixed wing UAV's inability to stay in the air in one place, it makes it unsuitable for under bridge inspections, which require the UAV to be able to maneuver in complex environments and stay in one place for data acquisition. The single rotor UAV is used instead of fixed wing UAVs when greater endurance or heavier payloads are needed. They are not commonly used because of their higher complexity, cost, and vibration. The multi rotor UAV is the most suited for structural inspection since it can hover in place and is maneuverable in complex environments. Additionally, they do not need a runway for takeoff like fixed wing UAVs, making them easier to deploy and land in crowded environments. Hybrid UAVs combine qualities of both fixed wing and multi rotor UAVs. They can cover long distances quickly and have the energy efficiency of a fixed wing UAV, while also being able to land and take off without a runway like a multi rotor UAV. For the methodology introduced in this thesis, a multi rotor UAV is required.

In recent years, the bridge inspection using small-scaled UAVs has been evaluated in laboratory-scale experiments as well as field demonstration [15, 16, 17]. UAVs enable safer,

economical, and less disruptive bridge inspection practice [2, 3]. The bridge inspection process using UAVs have five major components such as bridge information review, site risk assessment, drone pre-flight setup, drone-enabled bridge inspection and damage identification with 3D models and image processing [18, 19]. Typical sensors carried by drones for bridge inspection are visual camera [14], LiDAR [20] and infrared camera [21]. Inspection plans are made based on existing bridge drawings and Google Maps, which allow the identification of risky areas and obstacles for path planning. The structural models also assist the development of an effective path planning for optimizing the flight duration [20]. Damage identification is performed with a 3D model reconstruction and using image processing.

While UAVs have proven themselves as being a useful asset for structural inspection, they still have certain limitations that prevent them from fully replacing traditional inspections. Some of these issues include not being able to easily gather information about the structure via conventional nondestructive evaluation methods, challenges of path planning in complex geometries, GPS limitation underneath the bridge, and debris hiding the defects. Kocer et al. studied the performance of ultrasonic sensor attached to a waveguide and carried by UAVs for contact measurement and showed the possibility of ultrasonic measurement in difficult-to-reach areas [9]. Salaan et al. (2018) designed and tested UAV within a passive rotating spherical shell to maneuver inside the enclosed areas [22]. Kucuksubasi et al. developed a method for autonomous UAV flight within a GPS-denied area, crack detection, and revisiting identified cracks [23].

### 2.3.1 3D Reconstruction Applications

Popescu et. al. compared terrestrial laser scanning (TLS), close range photogrammetry (CRP), and infrared scanning (IS) and found that although TLS was the most accurate of the three techniques, the most cost-effective technique that was also still accurate was CRP as shown in Figure 4 [24]. Popescu et al. conducted a case study that evaluated the viability of

using 3D reconstructed models of bridges as an alternative to in person inspection [4]. It was found that while damage could be identified in the bridge models, the raw images provided the level of accuracy needed to make more complete observations. This was because the models did not have high enough texture quality and low enough distortions. Tscharf et al. explored how to obtain accurate 3D models and found that more images and the use of 7 or 8 ground control points improves model accuracy [25]. 3D views of bridge components can be connected with Bridge Information Modeling (BrIM) for more accurate estimate of the degradation effect to the bridge performance [26, 27]. Inzerillo et. al. determined the viability of 3D reconstruction for the evaluation of pavement distress [28]. It was found that using a Nikon D5200 camera at about 50 to 120 cm produced better results than a UAV with a GoPro Hero 3 camera at approximately 500 cm.

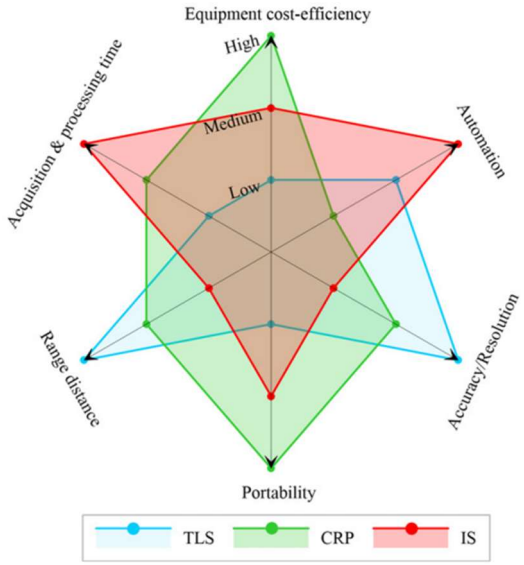


Figure 4. Performance of 3D imaging methods [24].

### 2.3.2 Guidelines for Successful 3D Reconstruction

2D images are converted into 3D models using the structure from motion (SfM) method by detecting the key points in each image and building a geometric connectivity by triangulation.

Therefore, it is important the subjects of 3D reconstruction have enough texture. Without sufficient texture the triangulation will fail because there are not enough key points. This can be an issue with some civil structures, especially those in newer condition, because the uniform surfaces may lack the number of key points needed for reconstruction. SfM thrives in randomness and as such, it may be best for future applications that structures be painted in ways that decrease the homogeneity of their texture. In a similar vein, there are surfaces that should be avoided when attempting SfM. These are reflective, shiny, or transparent surfaces. The reconstruction may fail or result in an inaccurate representation. While not an issue in the application of this thesis, it is important to remember that 3D reconstruction requires the subject to remain still throughout image capture. This makes capturing live subjects more difficult than inanimate objects.

According to the ContextCapture Guide for photo acquisition, it is recommended that a constant focal length is maintained and there is constant homogenous lighting to get the best results [29]. Digital zoom should never be used, and images should not be resized, cropped, or rotated in any way. Blurry photos, the use of a flashlight, and optical stabilization should be avoided. It should be noted that for the applications of 3D reconstruction photos should be taken with everything in focus, not just the subject. This means that images should have a large depth of field. Blurry photos refer to completely blurry and partially blurry cases. This situation would arise if images were taken with a shallow depth of field. In general, images should be captured with the aim of minimizing the amount of background while still capturing as much of the subject as possible. For the best quality 3D model, a camera with a large sensor and a high-quality lens is recommended.

Path planning is essential to inspect a structure and create a quality 3D model. ContextCapture's guidelines for photo acquisition are suggestions that do not need to be followed exactly, as actual data collection involves a lot of approximation and unless the

planned path can be automated, it is highly difficult to capture images perfectly. 70% overlap is recommended in general between images but if there is at least 50% overlap the reconstruction should be successful. It is recommended that angle differences between images should not exceed 15°. Distance from the subject is also a factor in successful reconstruction. Generally, images should be taken while maintaining the same working distance between pictures. If the working distance should be changed mid shoot, it should be done so gradually as a sudden change in photo resolution can lead to failure during triangulation. Recommendations for capturing aerial maps are different and are outside the scope of this thesis.

### 2.3.3 Image Processing Applications

The images collected by visual cameras can be processed further (e.g., image enhancement, spatial filtering, threshold segmentation, gradient-based edge detection) to recognize the presence of cracks, especially bridges made of concrete [30, 31, 32, 33]. Figure 5 shows an example of improving the contrast of hail damage on a shingle roof. The colorspaces used were RGB (red, green, blue), HSV (hue, saturation, value), YCbCr (brightness, blue chrominance, red chrominance), and L*a*b* (brightness, red-green tones, yellow-blue tones). As can be seen from the figure, different colorspaces perform better than others depending on the image. Figure 6 shows an example of extracting the area of corrosion from an image using the imcontour function in MATLAB. These techniques can be a useful tool for inspectors. The detection of fatigue cracks is difficult since they occur in hard to access under-bridge members. In addition, they are extremely short and narrow, so they are not easily visible. Dorafshan et al. evaluated the drone cameras and the required distances to be able to detect fatigue cracks [34]. Many methods have been developed for automated damage detection [35, 23, 36, 37, 38, 39, 40]. Specifically, Chen Q. et al. and Yundong et al. present automatic methods to detect corrosion in steel structures using image processing combined with deep learning [35] and image processing [39], respectively.

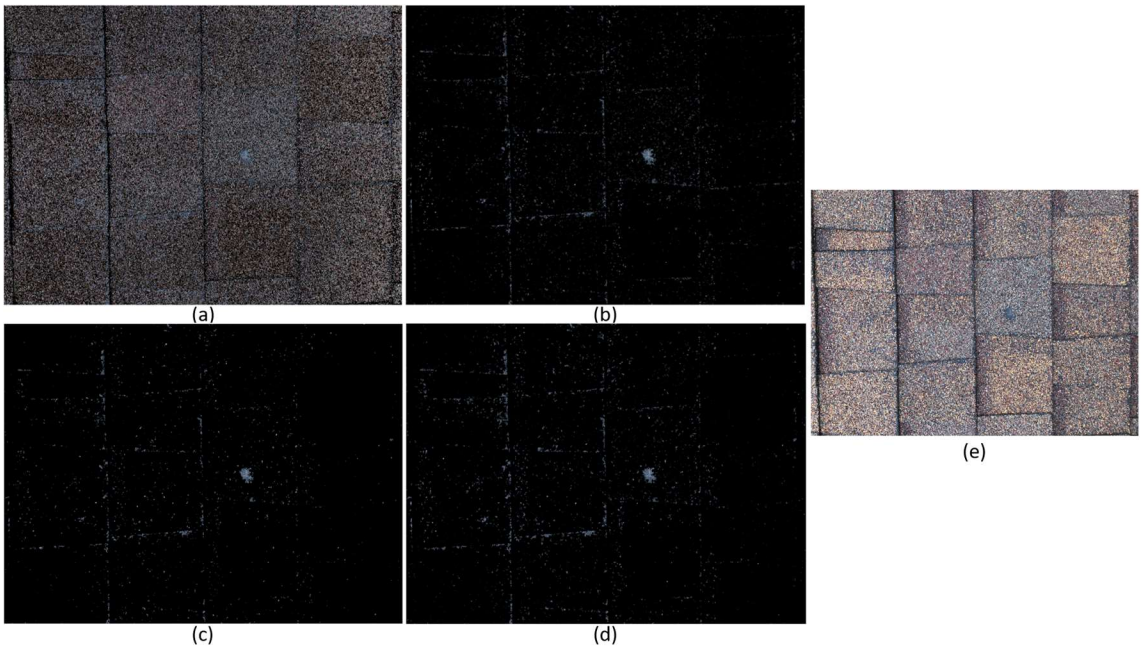


Figure 5. Using Color Thresholder from the Mathworks Image Processing Toolbox to improve contrast of hail damage to roof using various colorspaces. (a) RGB, (b) HSV, (c) YCbCr, (d) L*a*b*, (e) Original image.

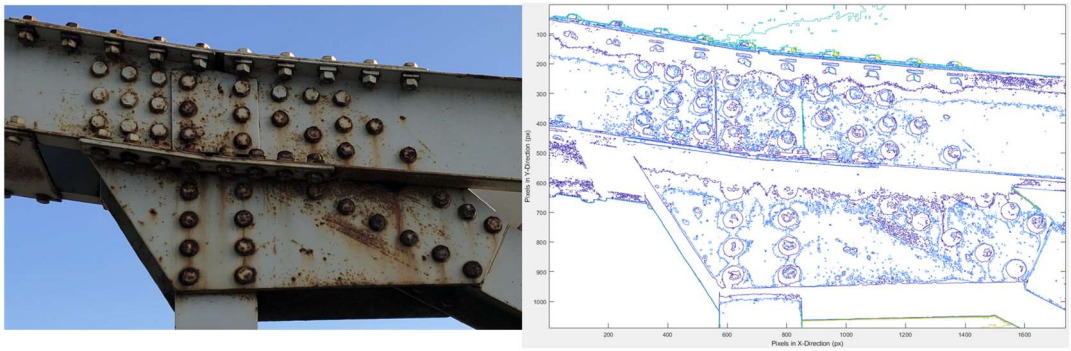


Figure 6. Using the imcontour function to extract areas of corrosion. (a) Original image, (b) Contours made using grayscale version of original image.

# 3. 3D RECONSTRUCTION OF STEEL GIRDER USING UAV

## 3.1 Introduction

This chapter includes a systematic data collection approach for maximizing the outputs of UAV inspection for geometric details and eliminating missing data points that lead to inaccurate 3D reconstruction. The 3D reconstruction of a W-shaped girder is built using the developed approach and the ad hoc data collection. Additionally, the chapter covers the application of image processing methods to evaluate the resolution of the UAV camera to capture different sizes of defects. The viability of the UAV images to observe the performance of passive sensors is discussed.

## 3.2 Methodology

For the UAV inspection of multi-girder steel bridges, there are certain geometric considerations that come into play including the number and spacing of girders, depth, width and length of girders, and bridge span. For the UAV and its camera payload, these are the UAV's safety distance, the camera's working distance, angular field of view, image resolution, number of pixels per feature resolution, UAV speed, and the time it takes for the camera to capture one image. Additionally, the desired percent overlap for the images should be known. For a successful 3D reconstruction, ContextCapture guidelines for photo acquisition suggest that the percent overlap should be no less than 50% and that angle differences between photos should not exceed 15°. Using these parameters, the proper measurement points to capture images can be determined. Table I outlines the variables used for calculating a safe and effective path plan for collecting images from a steel girder to build a high-resolution 3D reconstructed model.

Table I. VARIABLES FOR PATH PLANNING.

| | | | |
|---|---|---|---|
| $\alpha$ | Angular FOV (deg) | $captureTime$ | Time to capture 1 image (sec) |
| $safety$ | Safety distance (m) | $D$ | Depth of girder (m) |
| $fres$ | Feature resolution. Size of smallest feature that can be detected (mm) | $W$ | Width of girder (m) |
| $imres$ | Camera image resolution (px) | $L$ | Span of girder (m) |
| $fpix$ | Number of pixels per feature resolution (px) | $H$ | Headspace; offset between top flange of girder and bridge deck (m) |
| $user\_pctlap$ | Percent overlap between photos (%) | $S$ | Spacing between girders (m) |
| $speed$ | UAV speed (kph) | $G_N$ | Number of girders |
| $FOV$ | Field of view (m) | $wkdt$ | Working distance (m) |
| $SidePosV$ | Vertical distance from the deck to the UAV camera at side view position (m) | $wkdt'$ | Adjusted working distance (m) |
| $SidePosH$ | Horizontal distance from the edge of the left flange to the UAV camera at side view position (m) | $A1S, A2S, A3S$ | Camera angles for side view position with respect to the horizontal (deg) |
| $CorPosV$ | Vertical distance from the deck to the UAV camera at corner view position (m) | $A1C$ | Camera angle for corner view position (deg) |
| $CorPosH$ | Horizontal distance from the edge of the left flange to the UAV camera at corner view position (m) | $A1B, A2B, A3B$ | Camera angles for bottom view position with respect to the horizontal (deg) |
| $BotPosV$ | Vertical distance from the deck to the UAV camera at bottom view position (m) | $BotPosH$ | Horizontal distance from the edge of the left flange to the UAV camera at bottom view position (m) |
| $lap$ | Shared distance between the $FOV$ of two UAV positions at the desired percent overlap (m) | $hlap$ | Half of $lap$ (m) |
| $\Delta\lambda$ | Distance between measurement points (m) | $numVPI$ | Number of VPIs for one bridge span |
| $numPics$ | Number of pictures for one bridge span | $travelDistance$ | Total distance travelled by the UAV to complete the planned path for one bridge span (m) |
| $betV1$ | Vertical distance between side view position and corner view position (m) | $betH1$ | Horizontal distance between side view position and corner view position (m) |
| $betV2$ | Vertical distance between corner view position and bottom view position (m) | $betH2$ | Horizontal distance between corner view position and bottom view position (m) |
| $betGirders$ | Distance between adjacent side view positions of successive girders (m) | $travelTime$ | Total time needed for UAV to complete the planned path for one bridge span (sec) |

To obtain images of suitable quality for structural inspection, defects as small as possible should be able to be detected. It is selected as 2 mm in this research considering the physical limitation of existing drones. Knowing this, the needed working distance can be calculated with

$fres$ equal to 2 mm or to whatever size the smallest feature to be detected is. Figure 7 depicts the geometric variables. The following equations were developed for determining the working distance needed to achieve the desired feature resolution:

$$FOV = \frac{fres * imres}{fpix * 1000 \frac{mm}{m}} \quad (1)$$

$$wkdt = \frac{FOV}{2 * \tan\left(\frac{\alpha}{2}\right)} \quad (2)$$

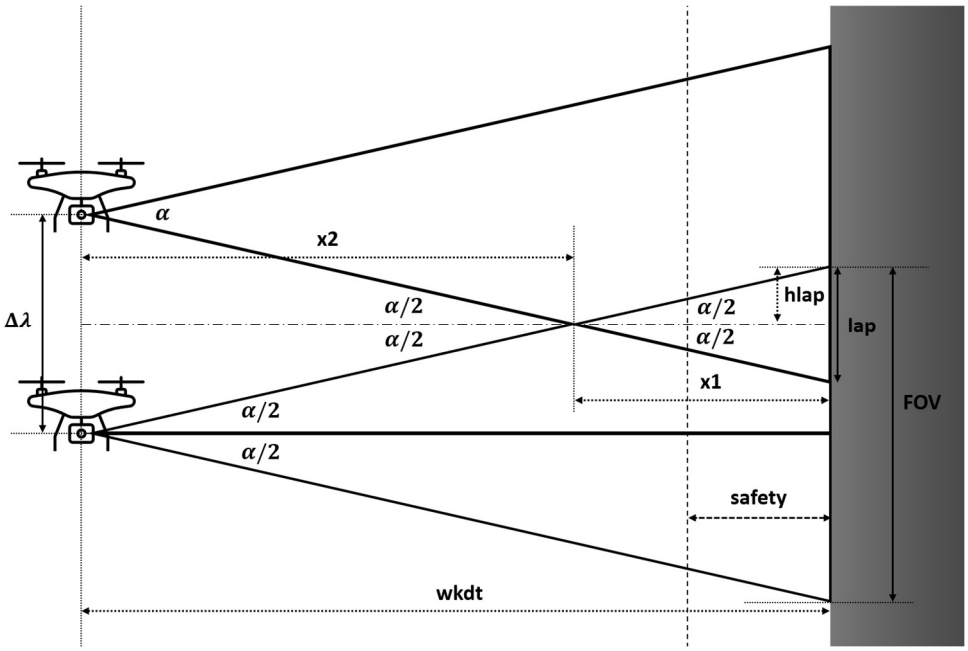


Figure 7. The geometric description of variables involved in calculating $FOV$ and Δλ. The working distance cannot be less than the safety distance in order to prevent accidents.

The following geometry checks are put into place to ensure that the UAV can fit between the spacing of girders and their depth from the bridge deck. This was determined using the safety distance in both lateral and vertical directions. In the lateral direction, the working distance compatibility to geometric constraints was also checked to see if the desired resolution for

images is possible. To follow the methods presented in this study, it is important that the UAV camera can be positioned at midway between the girder's top and bottom flanges and that at the very least the UAV's safety distance is not infringed by girder spacing.

The vertical positioning of the UAV from the girder of interest depends on the UAV's safety distance. The lateral positioning of the UAV from the girder of interest will depend on the desired working distance and existing constraints. Specific cases for both vertical and lateral checks are detailed in Figure 8 and Figure 9, respectively.

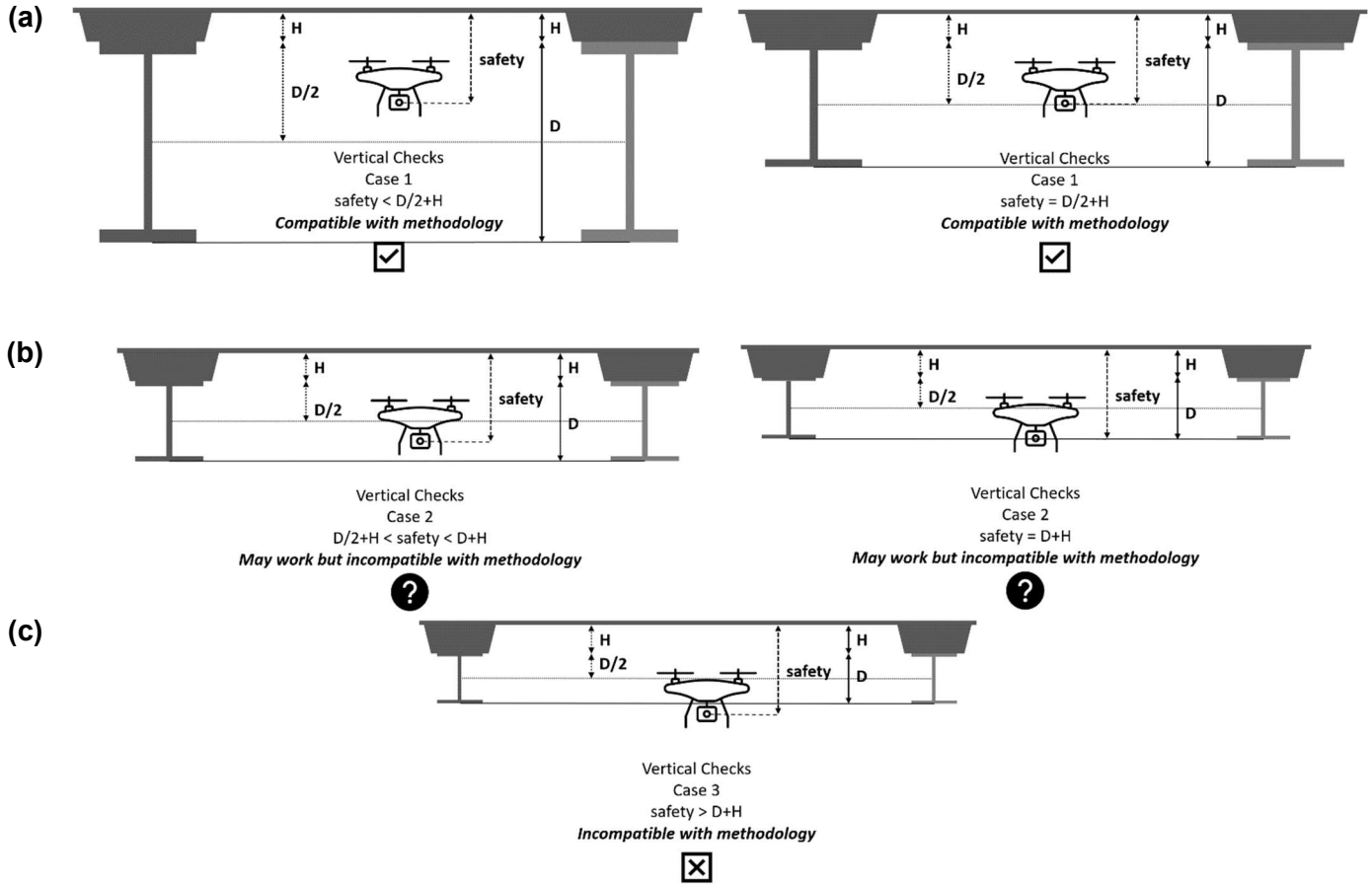


Figure 8. Vertical checks relative to girder height ($D$) and bridge deck ($H$). In the vertical direction, only safety distance is checked for clearance as no pictures are captured focusing on the bridge deck. (a) Case 1: $safety \leq \frac{D}{2} + H$, (b) Case 2: $\frac{D}{2} + H < safety \leq D + H$, and (c) Case 3: $safety > D + H$.

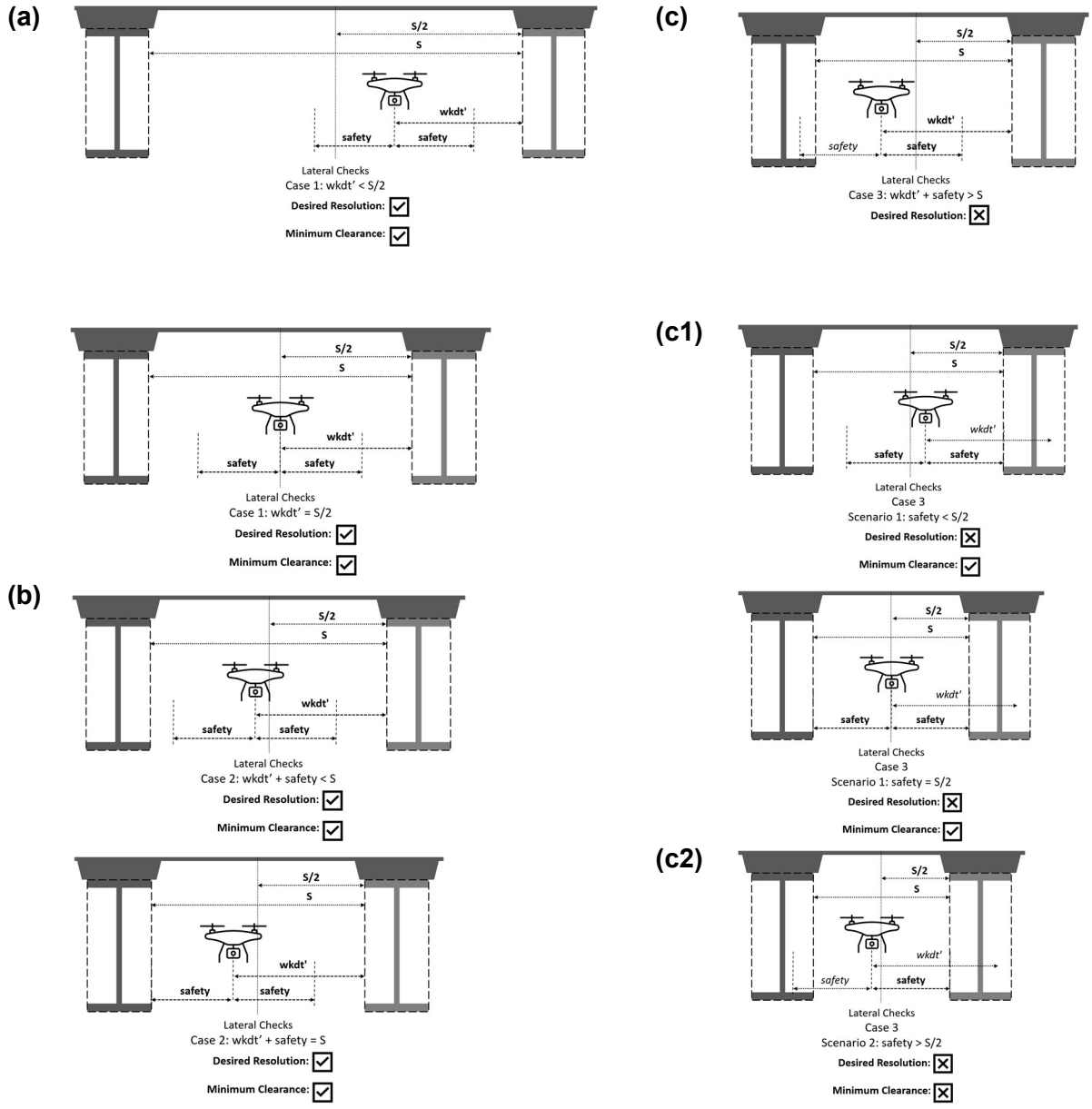


Figure 9. Lateral safety checks relative to spacing between girders ($S$) and girder width ($W$). Here, working distance ($wkdt$) is adjusted by subtracting half the flange width to get $wkdt'$. In the lateral direction, both working distance and safety distance are checked since images of the girder will be captured. Minimum clearance is determined by safety, whereas desired resolution is determined by working distance. (a) Case 1: $wkdt' \leq \frac{S}{2}$, (b) Case 2: $wkdt' + safety \leq S$, (c) Case 3: $wkdt' + safety > S$, (c1) $safety \leq S/2$, and (c2) $safety > S/2$.

The flight path position setup proposed is shown in Figure 10. It consists of two side views, two corner views and one bottom view. As shown in Figure 10(a), the plan is that the UAV should, at each position, go along the length of the girder taking pictures until reaching the end, then the UAV should switch to the next closest position and go along the length of the girder taking pictures until reaching the end, then the UAV should switch to the next closest position and go along the length of the girder again. This process would be repeated until all positions and angles at each position have been fulfilled before moving on to the next girder and repeating the process. Figure 10(b) and (c) depict the two possible scenarios of switching between girders and the general path across multiple girders in a cross-sectional view. When the UAV's working distance or, if being used instead, safety distance is less than or equal to half the spacing between girders the UAV will need to proceed to the next girder by moving toward the next girder as shown in Figure 10(b). When the UAV's working distance or safety distance is greater than half the spacing between girders the UAV will need to proceed by moving towards the previous girder when transitioning to the next girder as shown in Figure 10(c).

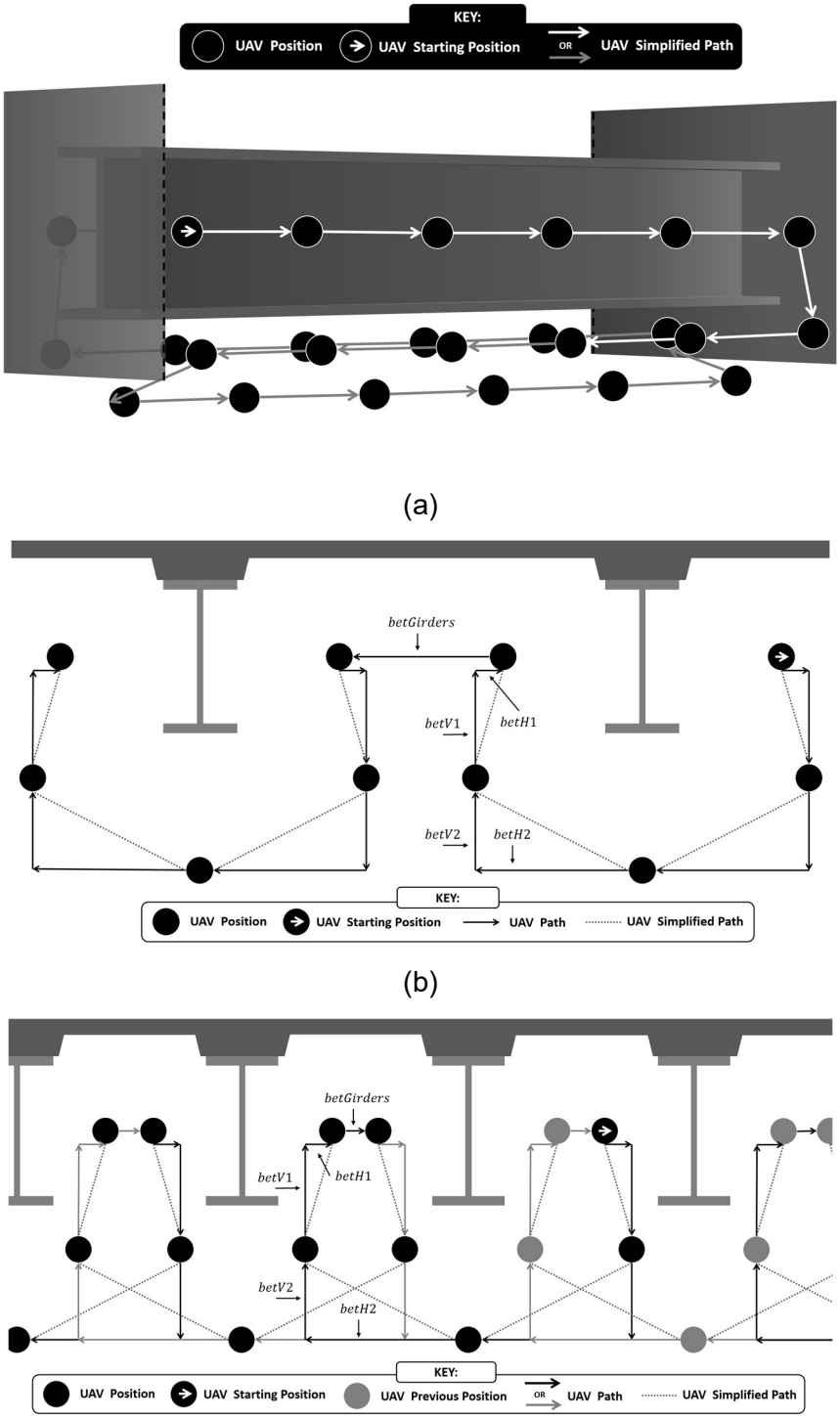


Figure 10. Proposed flight plan positions, (a) overall path of UAV, (b) cross-sectional view of path across multiple girders, when working distance is less than or equal to half the spacing between girders and (c) cross-sectional view of path across multiple girders, when working distance is greater than half the spacing between girders.

The side view is positioned at half the girder depth and consists of three angles. One angle is focused on the intersection between the top flange and the web, the next angle is focused straight on the web, and the last angle is focused on the intersection between the web and the bottom flange. The bottom view is directly centered beneath the girder which also consists of three angles. Two of the angles focus on the two opposite edges of the bottom flange and one focuses on the center of the bottom flange. The angles and each of their positions are shown in Figure 11. Calculations for the exact position and angle are shown in Table II. Depending on the geometry checks performed previously, $wkdt$, shown in the calculations in Table II will refer to either working distance or safety distance, $safety$. The corner view angle was defined as $15°$ and its purpose is to provide sufficient overlap for the side and bottom views.

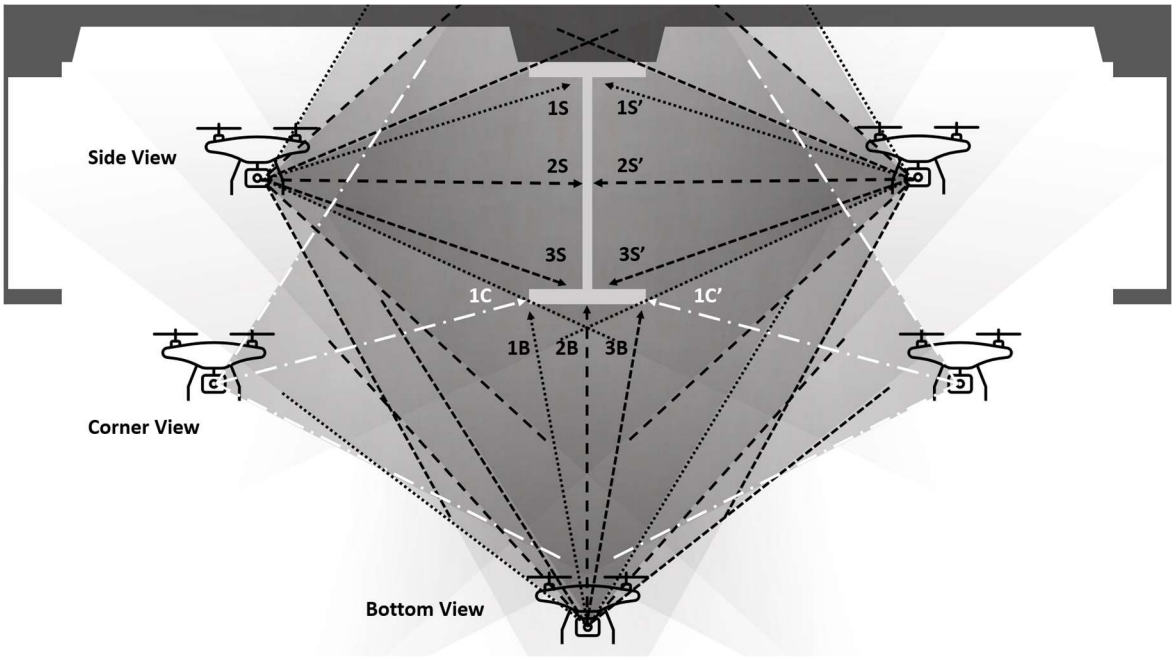


Figure 11. Depiction of proposed camera angles for each UAV positions.

Table II. CALCULATIONS FOR EXACT POSITION RELATIVE TO THE BRIDGE DECK AND THE LEFT EDGES OF THE GIRDER'S FLANGES AND EXACT CAMERA ANGLES RELATIVE TO THE HORIZONTAL. IF RESULT WAS CASE 3, SCENARIO 1, THEN $wkdt = safety$

| | |
|---|---|
| **Side View Position:**<br>$SidePosV = \frac{D}{2} + H$<br>$SidePosH = wkdt - \frac{W}{2}$<br> 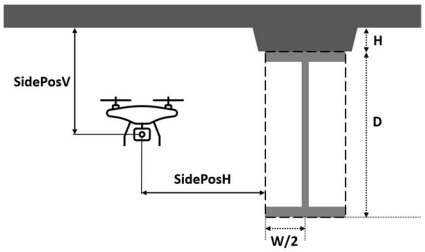 | **Side View Angles:**<br>$A1S = tan^{-1}\left(\frac{D/2}{wkdt}\right)$<br>$A2S = 0$<br>$A3S = -tan^{-1}\left(\frac{D/2}{wkdt}\right)$<br> 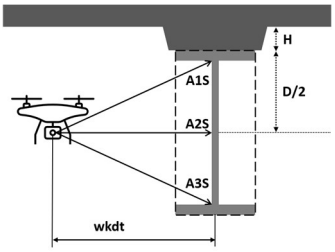 |
| **Corner View Position:**<br>$CorPosV = D + H + wkdt * \sin(15)$<br>$CorPosH = wkdt * \cos(15)$<br> 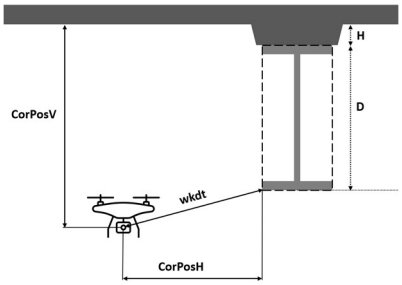 | **Corner View Angle:**<br>$A1C = 15°$<br> 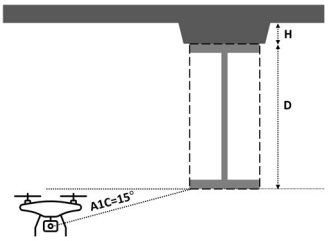 |
| **Bottom View Position:**<br>$BotPosV = wkdt + D + H$<br>$BotPosH = -\frac{W}{2}$<br> 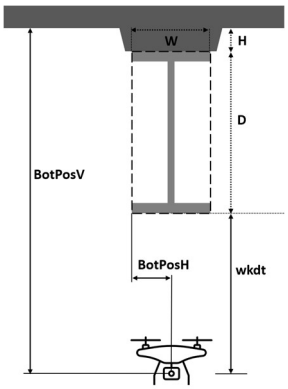 | **Bottom View Angles:**<br>$A1B = tan^{-1}\left(\frac{W/2}{wkdt}\right) + 90°$<br>$A2B = 90°$<br>$A3B = 90 - tan^{-1}\frac{W/2}{wkdt}$<br> 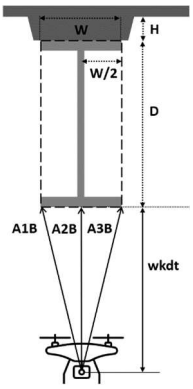 |

The distance between measurement points, $\Delta\lambda$, needs to be calculated to determine how many viewpoints of interest (VPIs) are needed. This distance only applies laterally, as the five vertical positions are set standard as previously calculated and do not change in this method. To determine $\Delta\lambda$, a desired percent overlap between photos must be defined. As mentioned previously, a percent overlap of at least 50% is recommended for 3D reconstruction. This is used to calculate $lap$, the shared distance between the $FOV$ of two UAV positions at the desired percent overlap, $user\_pctlap$. Then, the distance between the point of intersection in angles of view and the surface, $x1$, is found and used to determine the distance between the intersection between the angles of view and the UAV, $x2$. This is detailed in Figure 7, shown previously.

$$lap = user\_pctlap * FOV \rightarrow hlap = \frac{lap}{2} \tag{3}$$

$$\Delta\lambda = 2 * (wkdt - \frac{hlap}{\tan\left(\frac{\alpha}{2}\right)}) * \tan\left(\frac{\alpha}{2}\right) \tag{4}$$

To determine the number of VPIs ($numVPI$), the span of a girder is divided by $\Delta\lambda$ which yields the number of VPIs per pass. This is then multiplied by the number of positions there are, five, and the number of girders in question $G_N$.

$$numVPI = \frac{L}{\Delta\lambda} * 5 * G_N \tag{5}$$

To find the total number of pictures, the number of VPIs per pass, per girder is needed. For the side position, there are 3 pictures per VPI and there are two side positions per girder. For the corner position, there is only one picture per VPI and there are two corner positions. For the bottom position, there are 3 pictures per VPI and there is only one bottom position. As a result, the number of pictures would be as follows:

$$numPics = \left(\frac{L}{\Delta\lambda} * 3 * 2 + \frac{L}{\Delta\lambda} * 1 * 2 + \frac{L}{\Delta\lambda} * 3 * 1\right) * G_N \quad (6)$$

The total length of flight can be calculated by spatial positions of UAV as shown in Figure 10. The total distance and time of measurement can be calculated using Equations 7 and 8. The variables are defined in Table I and Figure 10.

$$travelDistance = G_N * 5 * L + 2 * (betV1 + betH1 + betV2 + betH2) + (G_N - 1) * betGirders \quad (7)$$

$$travelTime = \frac{travelDistance}{speed * 1000\frac{m}{km} * \frac{1\ hr}{3600\ s}} + numPics * captureTime \quad (8)$$

A full example of the calculations for this methodology for a single 42.70 m span of a bridge is worked out with sample inputs provided by the FHWA [41] as shown in Table III. The calculated variables using the equations described above are summarized in Table IV. The calculation is shown step by step in the appendix. The total travel time is calculated as 149 minutes. As typical flight times are about 20-30 minutes per UAV, the measurement can be taken by 5-7 UAVs (called multi-agent measurement) or multiple batteries to minimize the total duration of measurement [42]. With a girder depth of 1.75 meters, the camera angles $A1S$ and $A2S$ exceed ContextCapture's recommended 15° maximum angle difference by a large margin. This indicates that this methodology is only suitable for smaller girder depths and flange widths since maintaining a close-range distance to the girder is important for obtaining higher resolution images.

Table III. INPUTS VARIABLES FOR THE PATH PLANNING EXAMPLE OF A MULTI-GIRDER STEEL BRIDGE FROM FHWA DESIGN EXAMPLE [41].

| | | | |
|---|---|---|---|
| $\alpha$ | 84° | $captureTime$ | 1 sec |
| $safety$ | 0.31 m | $D$ | 1.75 m |
| $fres$ | 2 mm | $W$ | 0.51 m |
| $imres$ | 3078 px | $L$ | 42.70 m |
| $fpix$ | 4 px | $H$ | 0.0884 m |
| $user\_pctlap$ | 70% | $S$ | 3.66 m |
| $speed$ | 0.805 km/h | $G_N$ | 4 |

Table IV. CALCULATED VARIABLES USING THE METHODOLOGY DEVELOPED IN THIS STUDY.

| | | | | | |
|---|---|---|---|---|---|
| $FOV$ | 1.54 m | $CorPosV$ | 2.06 m | $betV1$ | 1.10 m |
| $wkdt$ | 0.855 m | $CorPosH$ | 0.825 m | $betH1$ | 0.23 m |
| $lap$ | 1.08 m | $BotPosV$ | 2.69 m | $betV2$ | 0.63 m |
| $\Delta\lambda$ | 0.462 m | $BotPosH$ | -0.255 m | $betH2$ | 1.08 m |
| $SidePosV$ | 0.963 m | $A1B$ | 106.61° | $betGirders$ | 2.46 m |
| $SidePosH$ | 0.6 m | $A3B$ | 73.39° | $travelDistance$ | 867.5 m |
| $A1S$ | 45.68° | $numVPI$ | 1850 | $travelTime$ | 132.5 min |
| $A3S$ | -45.68° | $numPics$ | 4069 | | |

### 3.3 Description of UAV and Experimental Subjects

The DJI Phantom 4 Pro was selected to record images as depicted in Figure 12. According to the DJI website, the camera payload specifications are 1-inch 20M CMOS sensor with Field of View as 84° and 8.8 mm/24 mm 35 mm equivalent size [43]. The image size was set as 16:9 with the pixel resolution of 5472x3078. Calibration sheets were used to test the resolution limits and as an aid for determining the dimensions of the girder and the pattern of the sheet. They were made by printing the pattern onto paper and bonding it to thin laser cut pieces of wood so that they could be reused for multiple trials of attachment to the girder at the web and flange locations. A total of five calibration sheets were created, each differing only by gap width. The gap widths used were 1 mm, 2mm, 3mm, 4mm, and 8 mm. The photos needed for 3D reconstruction were taken around the entire girder and processed using Bentley ContextCapture software. However, the photos for image processing were taken with the lens focusing only on

the calibration sheets, while slowly increasing the working distance. The image analysis was performed using the Image Processing Toolbox developed by Mathworks. A 2.58 m long steel girder with geometry like that of a HP8x36 was used for validating the methodology and extracting the minimum distance required for capturing the details of typical steel girders.

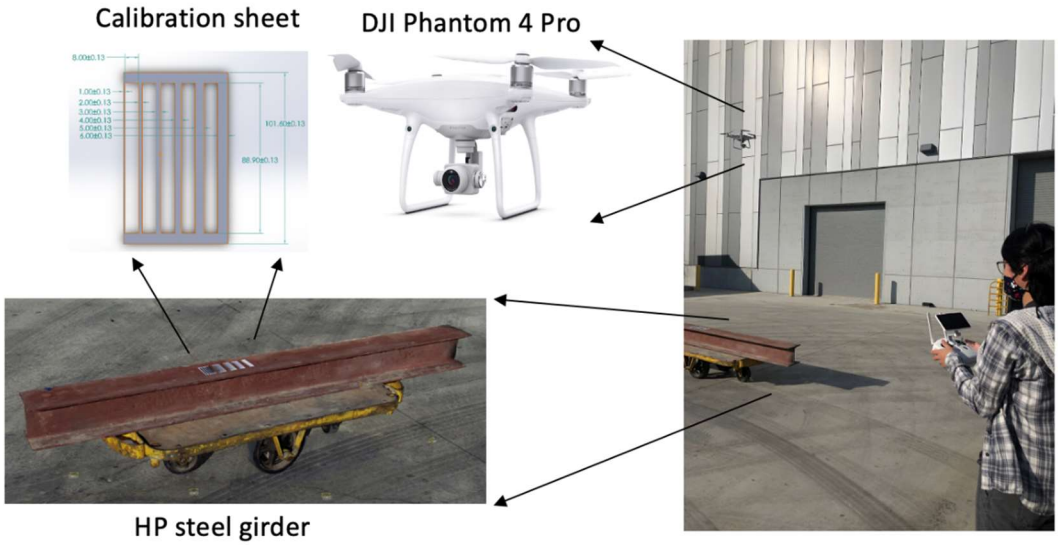


Figure 12. The components of experimental setup: steel girder, calibration sheet and DJI Phantom 4 Pro.

### 3.4 Data Collection

The calibration sheets were attached to the girder's web for some trials and its flange for other trials. Data collection occurred over the course of multiple days as photos from each attempt needed to be processed to determine the quality of the 3D reconstruction model that could be obtained from each set. Images were captured by manually operating the drone. The specifications of data sets are presented in Table V. For 3D reconstruction, photos need to be taken at multiple angles and elevations around the girder. From 3D reconstruction results, percent error was able to be calculated using the known geometry of the calibration sheet and, for the final trial, marks drawn onto the girder itself. From 3D reconstruction results, a percent

error vs. number of photos plot was created which helped to visualize the effectiveness of each data collection trial. For assessing the image resolution, the images were taken from an orthogonal view of the calibration sensors at different working distances. Since the dimensions of calibration lines were already known, the percent error was able to be calculated between the actual and experimental values.

Table V. THE SPECIFICATIONS OF UAV DATA SETS.

| Data Set | Date | Weather | Number of images captured | Method and elevations images captured |
|---|---|---|---|---|
| 1 | October 21, 2020 | Partly cloudy | 55 | Ad hoc data collection at middle view |
| 2 | November 4, 2020 | Overcast, windy | 28 | Ad hoc data collection at middle view |
| 3 | November 6, 2020 | Clear, sunny | 115 | Ad hoc data collection at profile view |
| 4 | November 11, 2020 | Partly cloudy | 332 | Ad hoc data collection at top, middle and profile views |
| 5 | March 26, 2021 | Overcast | 43 | Using the proposed methodology |
| 6 | June 1, 2021 | Clear, sunny | 15 | Image processing dataset |

### 3.5 3D Reconstruction Accuracy

3D reconstruction accuracy in this section was explored in this section to determine the level of qualitative and quantitative accuracy that could be attained using the specified UAV and camera. After completing four ad hoc trials, the methodology described next was tested and compared to ad hoc trials. Results in this section reveal best practices found for the case of creating photogrammetric models of steel girders.

### 3.6 Results

Results of the 3D reconstruction methodology were evaluated qualitatively and quantitatively. Qualitative results are for evaluating distortions in the model and texture quality.

Quantitative results are for geometric measurement accuracy. Both types of results are important for evaluating the viability of the model for structural inspection.

### 3.6.1 Shadow Effect and Detailing of Planar Dimensions

In this section, the 3D models were evaluated qualitatively to assess the influences of shadow to images. Figure 13 depicts the position of the relative elevations as reference to the first four reconstructed image sets. The elevations for the data set 5 were based on the methodology described in the previous section. Figure 14 shows the camera positions for each attempt as well as the number of photos used in each model, elevations used and notable weather conditions.

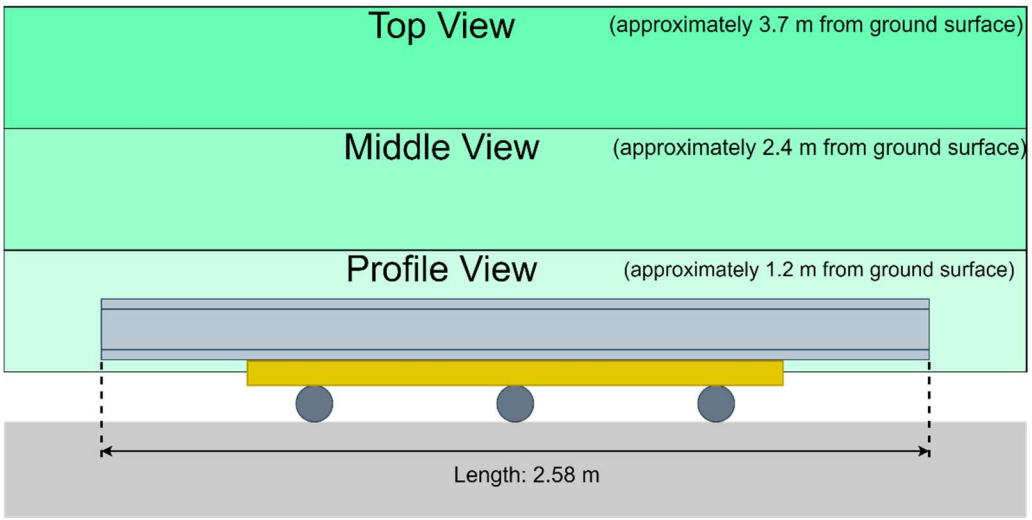


Figure 13. Depiction of relative drone elevations.

Figure 15 and Figure 16 show the oblique views and the side views of 3D constructed models. The first data set made on consisted of 55 images. This model had the fewest number of holes of all the models. The second data set consisted of only 28 photos, the fewest of all the attempts. An effort was made to try and maintain consistent overlap, get closer, and go around the girder in a more organized way. This model had the highest number of holes at flanges and webs due to insufficient data points to connect planar data. The third data set consisted of 115

photos. In this attempt, all photos were taken profile to the girder, even closer, and in greater quantities. This was done to obtain clearer shots of the areas that have consistently been distorted, improve texture, and to avoid holes. This model had the most holes of all the other models. To improve in this area, it was determined that more elevations were needed. While initially it was thought that more images at one elevation would be sufficient, the results from this attempt have shown that this is not the case. The fourth data set consisted of 332 pictures, the most of all the attempts. For this attempt, photos were taken approximately as close to the girder as the previous attempt and at multiple elevations. The results for this model were the best of all the attempts in terms of holes, distortion, and texture. There were much fewer holes as compared to previous attempts. In the final and fifth data set, the proposed methodology was used as a guide to collect 43 images. Styrofoam blocks were attached to the ends of the girder to simulate the confinement that would be faced during an inspection at an actual bridge, and this would be the only model with the ends confined. The results for this model had no holes that cut completely through the girder flange found in previous data sets. There were also no holes on the web in this model.

In addition to smooth texture extraction from the 3D reconstructed images, shadow influences the connectivity of flange and web joints. Figure 17 and Figure 18 show the end views of 3D constructed models with and without texture, respectively. Texture observations are shown in Figure 19. Since the fifth data set had the ends covered, the model ends are shown as a cross section from the model itself from each side, obtained by running the ContextCapture model again but with a smaller bounding box. The distortions of data set 1 introduced the concept of distortions that followed the shadow cast by the girder's flanges, and as such it was dubbed the shadow effect. The data collected on data set 2 resulted in the most distorted model likely due to insufficient images. The downgrade in texture in both the flange and the web was attributed to the fact that it was windy on this day. It was concluded that it might be possible to

mitigate the shadow effect by taking images with the camera oriented profile to the girder. It was also determined that more pictures, as in more camera positions and angles, may help reduce the number of holes as the previous attempt did better in this area. When these ideas were applied in the following datasets, the shadow effect was very minimal. The fifth data set displayed minimal shadow effect but did not perform as well as data set 3 and data set 4 in this area. Notably, data set 5 had the best texture quality of all 5 models and this can be distinctly seen when observing the bottom flanges of each model.

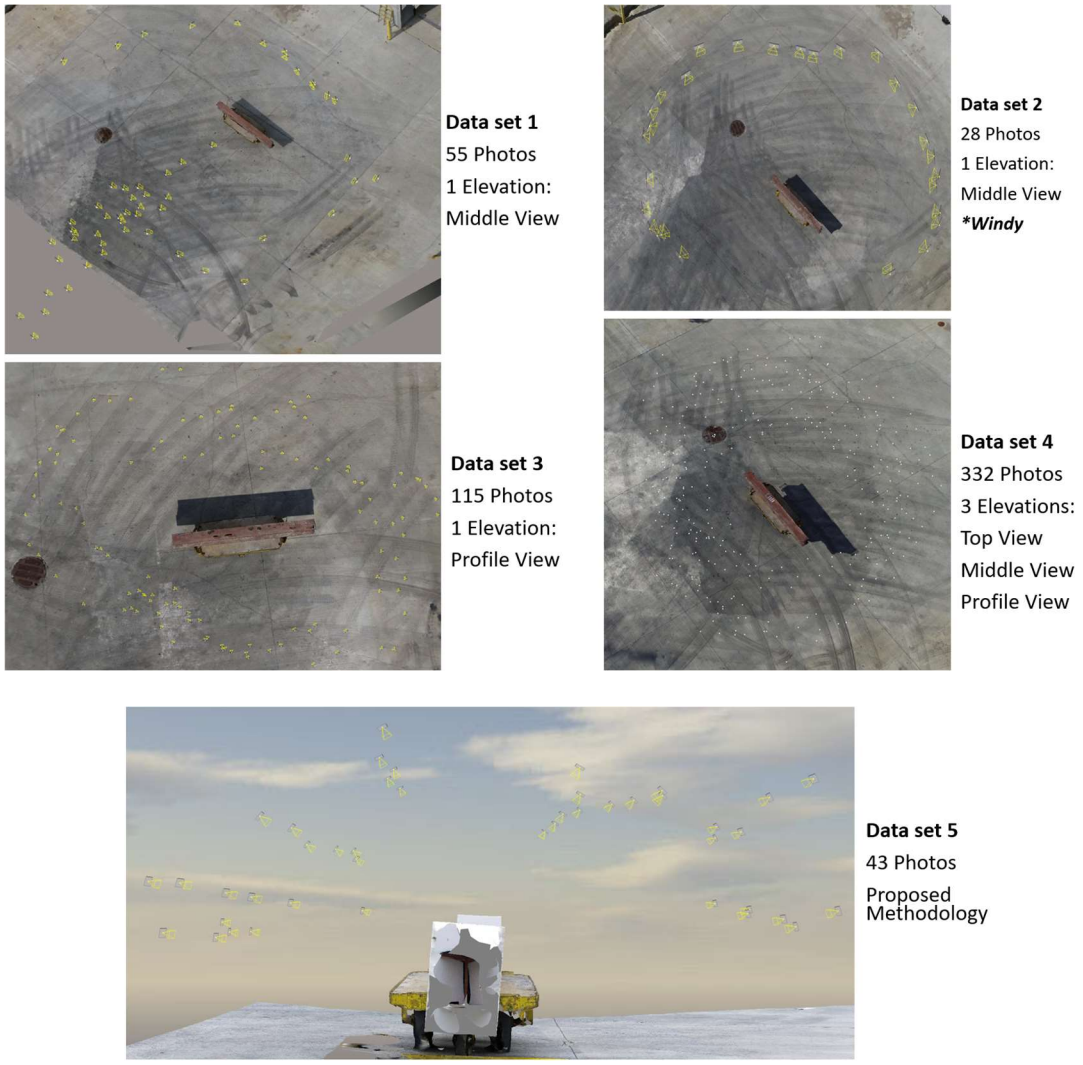


Figure 14. Camera positions of five data sets.


Figure 15. Oblique views of 3D constructed images showing holes on flanges.

Data set 1

Data set 2

Data set 3

Data set 4

Data set 5

Figure 16. Side views of 3D constructed images indicating holes on the web.

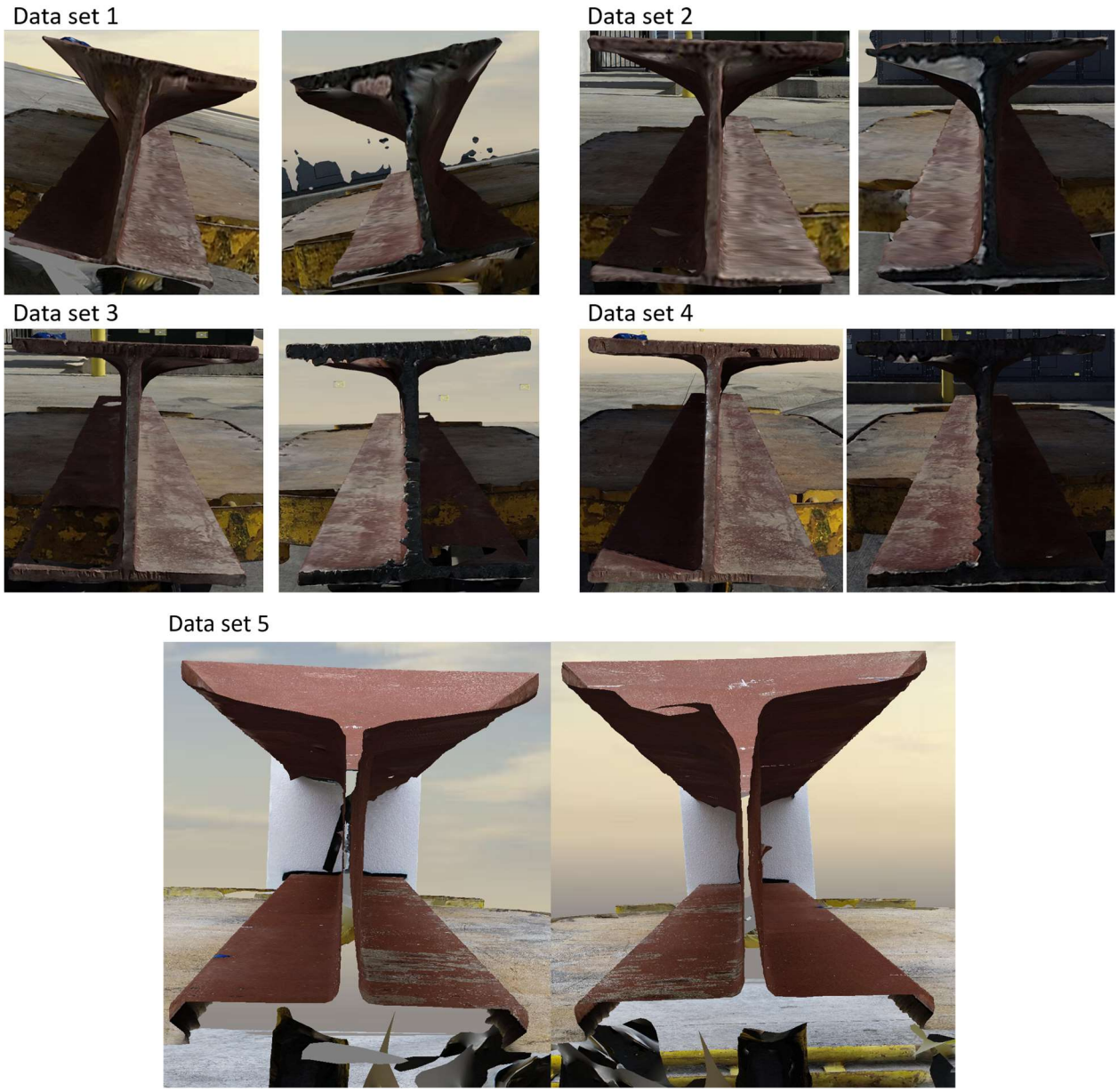


Figure 17. End views of the girder in each of the four models with texture on. Shadow effect prevents a clear definition of web-flange connection.

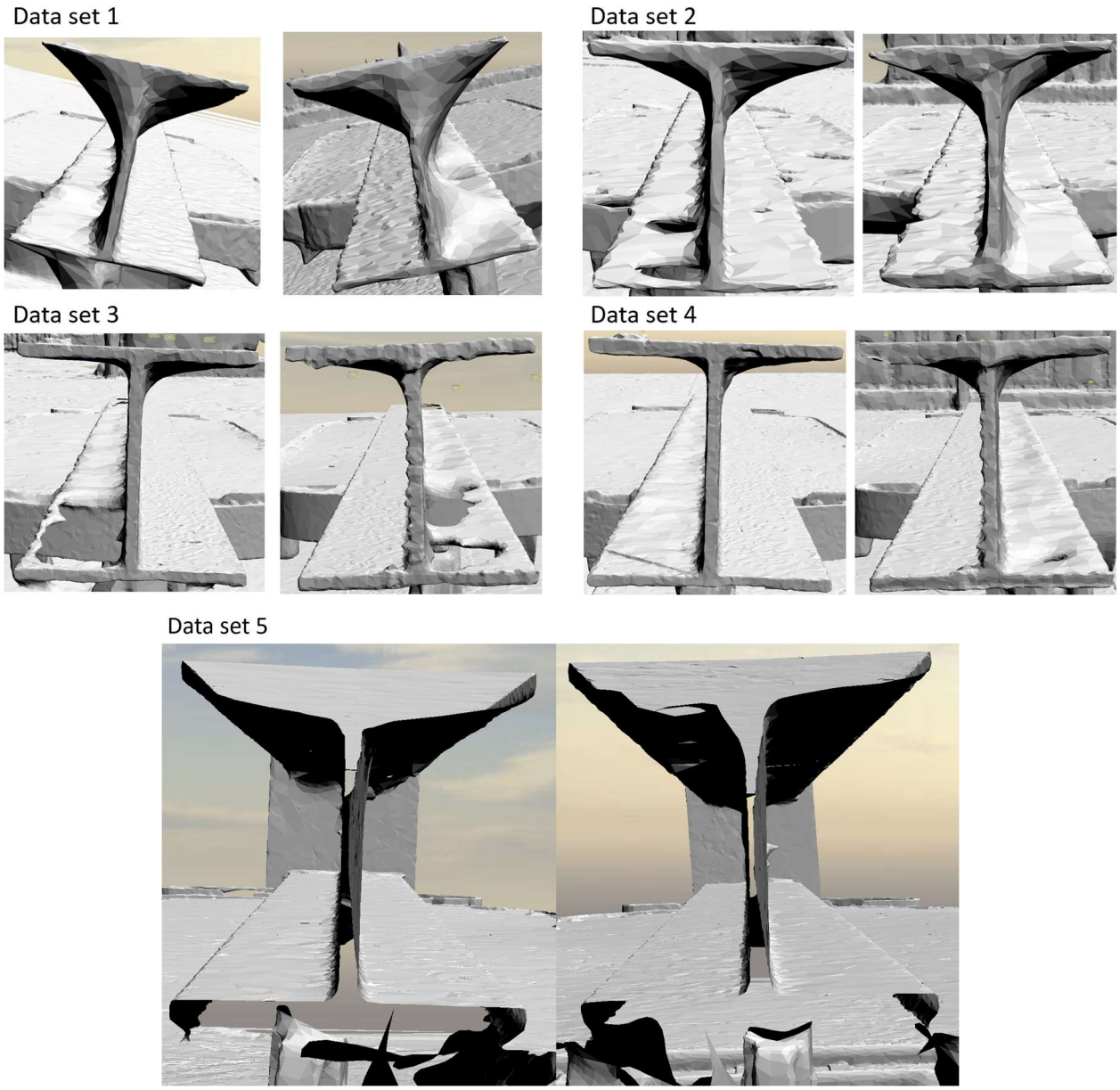


Figure 18. End views of the girder in each of the four models with texture off.

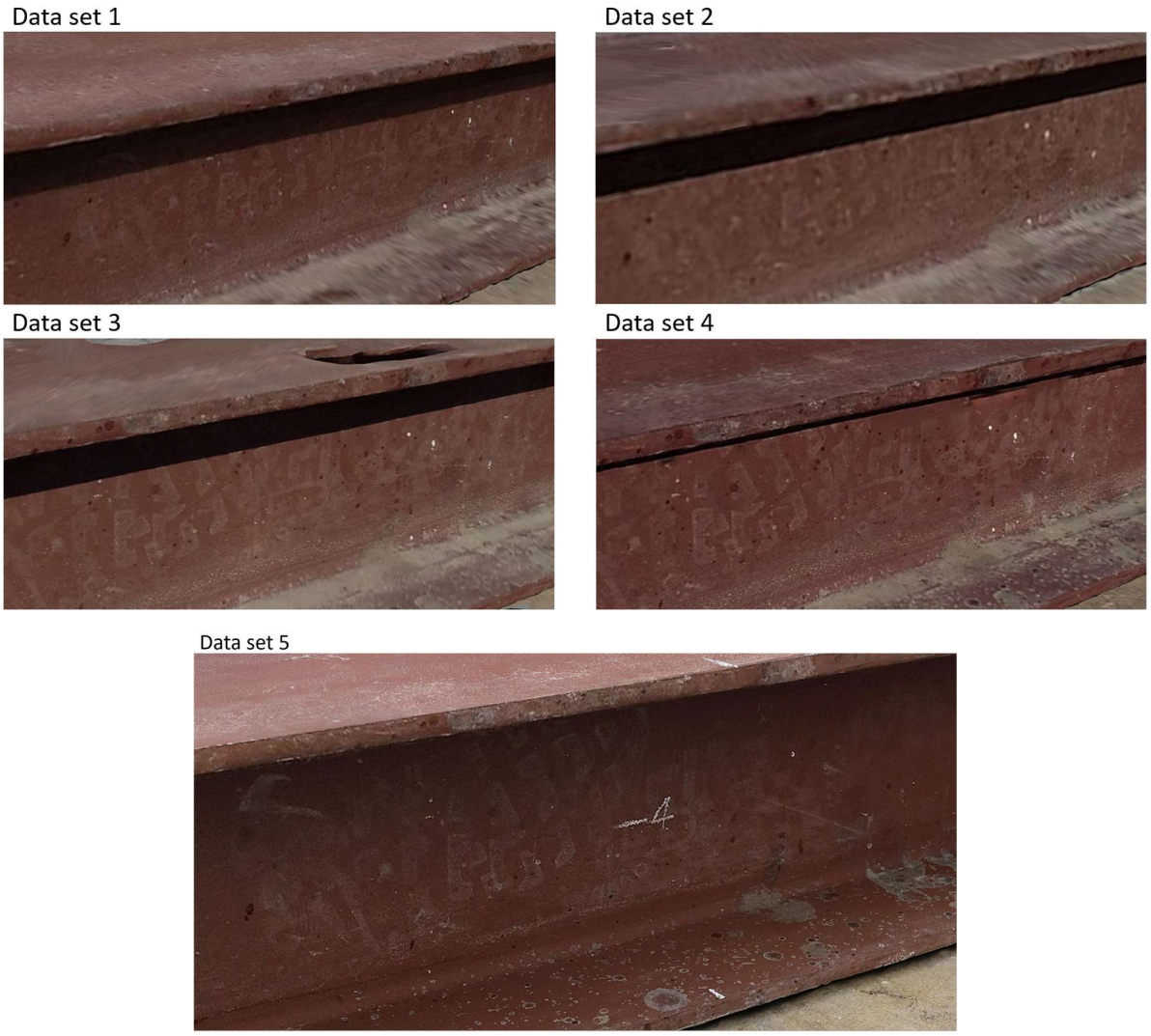


Figure 19. Texture details of all four models to extract paint quality and localized defects.

Overall, the main issues encountered were holes, distortions, and low texture resolution. To avoid holes, it was determined that multiple camera angles and elevations helped the most. To reduce distortions, the best practice was to make sure that pictures were taken as profile to the girder and as close as possible. The success of the data set 5 suggests that taking photos up close for all surfaces of the girder was the most influential factor to improve texture. While the data set 4 had the most pictures, many that involved the bottom flange were taken far away. The data set 5 had images of the bottom flange up close within its image set, as the pictures were taken with the intention of maintaining a consistent working distance from all angles. Other

texture trends were that the texture improved when there was no wind and the least model distortions.

### 3.6.2 Geometric Resolution of 3D Reconstructed Images

To determine the accuracy of the 3D reconstructed model, the calibration sheets were used to create a conversion factor to convert the arbitrary model units to millimeters for comparison to the actual dimensions of the girder. The actual physical quantities were a flange thickness of 9.53 mm, web thickness of 9.53 mm, flange width of 206.38 mm, girder height of 206.38 mm and a girder length of 2581.28 mm. Table VI shows the results of the measured physical quantities and the errors. Looking at the overall accuracy, the model that performed the best in this area was data set 4 with the percent error coming in at 5.92%. This data set had the greatest number of photos of all data sets. The most poorly performing model was data set 2, coming in with a percent error of 55.54%. This data set had the least number of photos of all data sets used for 3D reconstruction. The data set 1 and data set 3 models had an overall percent error of 51.74% and 41.09%, respectively. The data set 5 model had an overall percent error of 32.82%. This data set was collected using the proposed methodology. When comparing the datasets solely based on percentage of error without consideration of the number of photos used, the methodology data set results do not stand out. When number of photos are considered, this is where the difference can be seen.

Figure 20 shows the effectiveness of each trial. The aim is to try and produce the highest quality model with the fewest number of images. The first four trials followed a linear trend which was expected as the techniques were somewhat similar in nature. The fifth model deviated from this trend, producing the best accuracy of all the data sets that used less than 332 pictures. This shows that the methodology has potential to provide better results with fewer photos than the previous test runs that were run under a more idealized situation without the confinement of the ends.

Table VI. MEASURED PHYSICAL QUANTITIES AND ERRORS.

| Data Set | Measured Quantity | | | | |
|---|---|---|---|---|---|
| | Flange thickness (mm) | Web thickness (mm) | Flange width (mm) | Girder height (mm) | Girder length (mm) |
| 1 | 10.96 | 8.65 | 221.72 | 227.72 | 2832.00 |
| 2 | 11.04 | 12.20 | 214.41 | 215.57 | 2663.51 |
| 3 | 11.65 | 11.22 | 207.58 | 206.71 | 2586.73 |
| 4 | 9.88 | 9.41 | 204.61 | 206.49 | 2579.51 |
| 5 | 10.01 | 12.02 | 205.54 | 207.79 | 2592.62 |

| Data Set | Errors | | | | |
|---|---|---|---|---|---|
| | Flange thickness (mm) | Web thickness (mm) | Flange width (mm) | Girder height (mm) | Girder length (mm) |
| 1 | 15.07% | 9.19% | 7.44% | 10.34% | 9.71% |
| 2 | 15.90% | 28.10% | 3.89% | 4.45% | 3.19% |
| 3 | 22.33% | 17.80% | 0.58% | 0.16% | 0.21% |
| 4 | 3.70% | 1.23% | 0.85% | 0.06% | 0.07% |
| 5 | 5.13% | 26.16% | 0.41% | 0.69% | 0.44% |

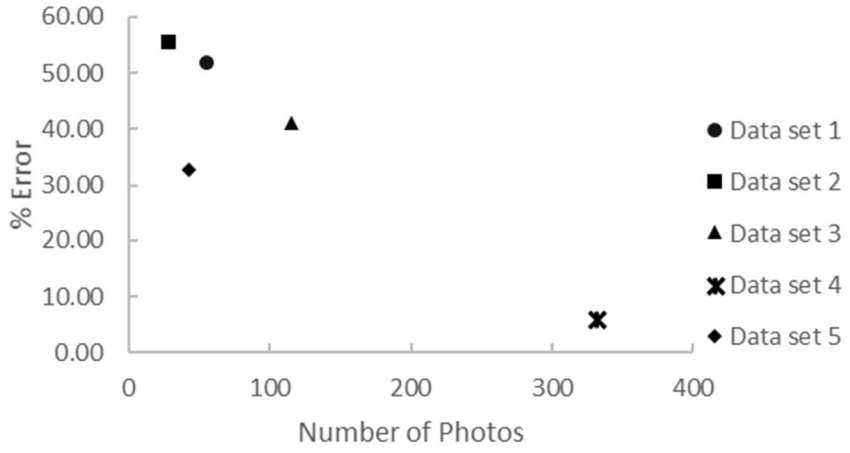


Figure 20. Influence of number of photos to total percentage of error, showing the effectiveness of each trial.

### 3.7 Image Processing Accuracy

Image processing accuracy was explored in this section to determine if the UAV's camera would be able to potentially see a broken passive sensor and to determine in general, the qualitative and quantitative observations that could be made using 2D images from this payload.

The passive sensor design and experiments will be covered in the next section. Based on these results, goals for the resolution of 3D model texture can be identified and used for comparison in future 3D reconstruction tests.

### 3.7.1 Data Extraction

The images of the calibration sheet were taken by the UAV camera at various working distances ranging from 1.83 to about 3.74 meters at two different locations. The objective of this experiment was to observe the impact of defect location on a girder to image resolution and accuracy of defect measurements. The image processing methods to improve the quality of images captured by the drone camera have been studied in literature [30, 39]. In this study, the overall image processing tools used in the Mathworks Image Processing Toolbox were the image viewer app, color thresholder app, and binary mask. Figure 21 shows how images were processed for resolution observations. The original image was cropped down to show only the area of interest using the image viewer app. Then, the color thresholder app was used to create a mask. The color space used was the L*a*b* as this produced the most consistent results for the images used in this experiment. For each calibration sheet location, the masks were made using the same thresholds to maintain consistency between photos and to simulate the batch processing of images.

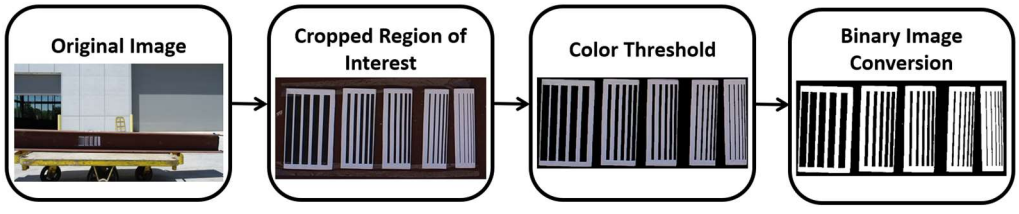


Figure 21. Image processing steps.

To collect quantitative information from the images, a conversion factor was made using the width of the 8 mm gap calibration sheet for each image used. For the first test, the gap width was taken in pixels from each image at five different locations along the line length, as shown in

Figure 22. These were converted using the previously created conversion factors for their respective images to get the gap width in millimeters. The standard deviation of the five measurements was taken for each image's data set to observe if light and image processing would have an influence on the consistency of measurements. Results are shown in Table VII.

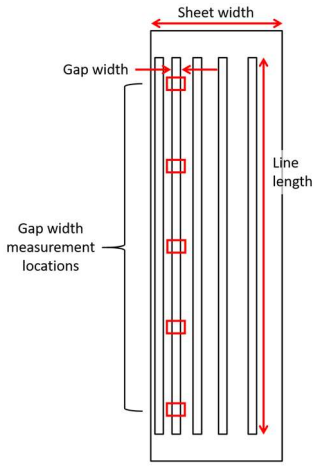


Figure 22. Measurements taken from images and general location of the five gap width measurements taken.

### 3.7.2 Results

The processed images of the two data sets are in Figure 23 and Figure 24. The top row of images are the masked and binary converted images. The bottom row of images is the cropped image before any effects were applied. Both the web and the flange images were taken on the same day and are from data set 6 as shown in Table V. Looking at the results of this experiment, one can see that the calibration sheet images on the web form jagged edges immediately while the calibration sheet images on the flange form jagged edges later as the distance increases. Jagged edges show the loss of detail in the images. Beyond just the increase in distance, this quality difference was attributed to the levels of light available at each location. The images on the web had calibration sheets in the shade and the images on the flange had calibration sheets in direct sunlight. Images in shade lost detail faster as distance increased than images in direct sunlight.

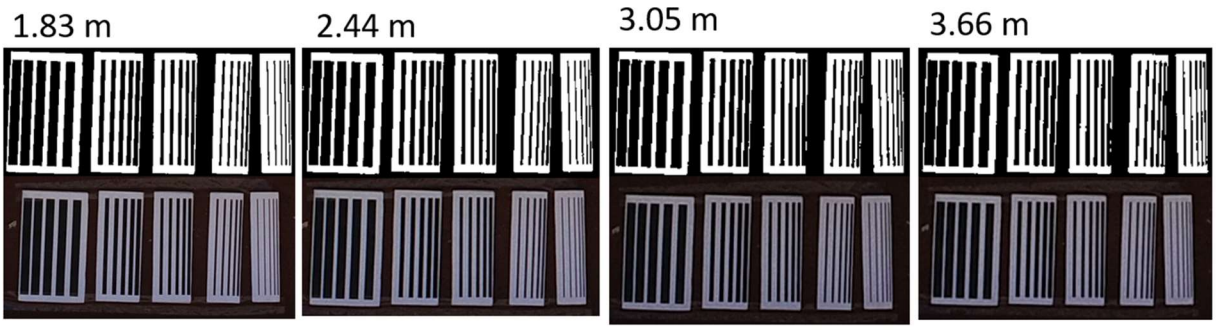


Figure 23. Results from calibration sheets located on web.

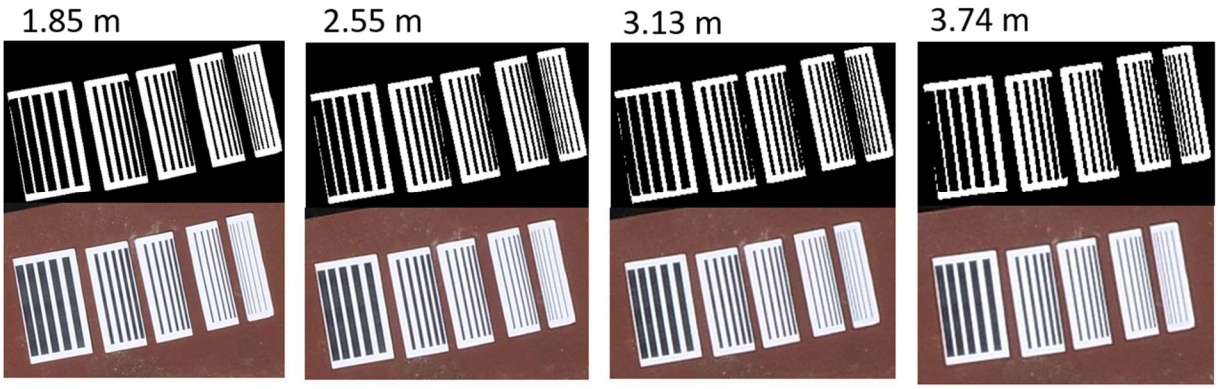


Figure 24. Results from calibration sheets located on flange.

From Table VII it can be seen that the calibration sheet images that were taken in direct sunlight, such as those on the flange, had an almost consistently lower standard deviation than the calibration sheet images that were taken in the shade, such as those on the web, for both unprocessed and processed images. This indicates that having direct sunlight helps maintain measurement consistency. For both the flange and the web, processed images almost always had a higher standard deviation than the unprocessed images. This may indicate that applying a binary mask oversimplifies the image, causing a loss of detail that interferes with measurements. A different image processing method may yield better results. Also, instead of using the same processing settings for each image, the use of more custom fitted settings for each picture may yield better results.

Table VII. A COMPARISON OF STANDARD DEVIATIONS BETWEEN FIVE 2 MM GAP MEASUREMENTS TAKEN ALONG THE LINE LENGTH AT DIFFERENT DISTANCES.

| **WEB:** | | | | |
|---|---|---|---|---|
| distance | 1.83 m | 2.44 m | 3.05 m | 3.66 m |
| unprocessed | **0.18** | **0.26** | **0.33** | **0.35** |
| processed | **0.36** | **0.40** | **0.47** | **0.64** |
| **FLANGE:** | | | | |
| distance | 1.85 m | 2.55 m | 3.13 m | 3.74 m |
| unprocessed | **0.08** | **0.12** | **0.27** | **0.31** |
| processed | **0.27** | **0.37** | **0.47** | **0.61** |

Each converted gap measurement was then compared to the actual gap distance of 2 mm to obtain a percentage of error for each. The percentages of error for each of the five measurements taken per picture were then averaged and are shown in Table VIII. For a comparison of measurements at different scales, a similar process was done for the line length. The conversion factor was used to convert the measured line lengths from pixels to millimeters and those values were compared to the actual line length to determine percentage of error. The results of this process are shown in Table IX.

It is observed that there is a significant difference in accuracy depending on the scale of the measurement. While the 2 mm gap width measurements resulted in 10-30% error, the 90 mm line length measurements resulted in only 0-3% error. This indicates that larger measurements can be reliably taken using image processing but that smaller measurements cannot be taken with the same accuracy. To find the smallest measurement length that could be accurately measured using only images and images that had been processed, a more in-depth experiment would be needed that encompassed measurements of more incremental lengths.

Table VIII. A COMPARISON OF THE AVERAGE PERCENT ERROR TAKEN FROM THE FIVE 2 MM GAP MEASUREMENTS TAKEN ALONG THE LINE LENGTH AT DIFFERENT DISTANCES.

| | distance | 1.83 m | 2.44 m | 3.05 m | 3.66 m |
|---|---|---|---|---|---|
| Web | unprocessed | **12.09** | **22.47** | **18.34** | **19.43** |
| | processed | **14.25** | **16.92** | **23.60** | **25.45** |
| | distance | 1.85 m | 2.55 m | 3.13 m | 3.66 m |
| Flange | unprocessed | **22.35** | **23.57** | **10.48** | **16.06** |
| | processed | **11.05** | **18.08** | **20.04** | **36.13** |

Table IX. A COMPARISON OF THE PERCENT ERROR FOR LINE LENGTH MEASUREMENTS AT DIFFERENT DISTANCES.

| | distance | 1.83 m | 2.44 m | 3.05 m | 3.66 m |
|---|---|---|---|---|---|
| Web | unprocessed | **0.22** | **0.57** | **0.32** | **0.42** |
| | processed | **0.09** | **0.79** | **0.08** | **2.74** |
| | distance | 1.85 m | 2.55 m | 3.13 m | 3.66 m |
| Flange | unprocessed | **0.33** | **1.63** | **1.39** | **2.90** |
| | processed | **1.07** | **0.33** | **2.47** | **1.77** |

# 4. DEVELOPMENT OF PASSIVE VISUAL SENSOR

## 4.1 Introduction

By creating a way to amplify the visibility of damage to a structure, visual inspection can provide more insight with less intervention and UAVs could provide more information about a structure during missions. Creating a mechanical passive sensor that could indicate localized steel yielding came as an idea to do just that. In the event of an overload or a collision, sensors attached throughout the length of a girder could help inspectors see the extent of damage and propose a more optimized solution for the situation. Figure 25 shows the process used to develop the passive sensor proposed. The inputs and output for modeling in ANSYS Static Structural are shown along with those for the experimental tensile tests.

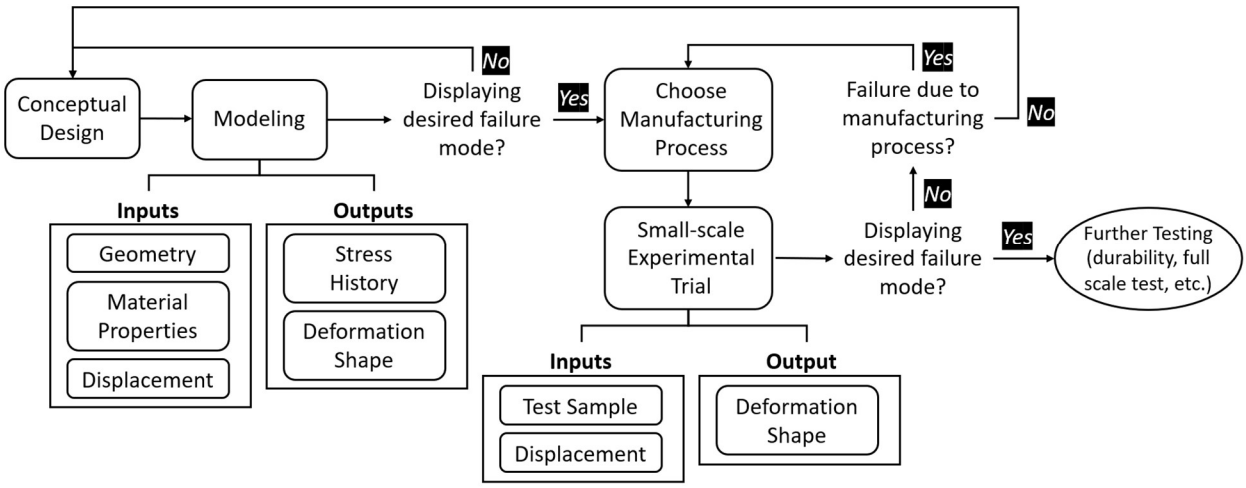


Figure 25. Flow chart of input-output relationship between numerical and experimental studies to design the passive visual sensor.

## 4.2 Sensor Design and Numerical Models

The overall objective was to choose a geometry that would allow the sensor to break in the event of a plastic deformation at the main structural element. Two concepts of sensor geometries were studied as shown in Figure 26. The first concept, shown in Figure 26(a), was made such that different levels of stress could be indicated in one part. The strands would be

fine-tuned to break incrementally at different levels of strain in the structure, showing the extent of damage. The second concept, shown in Figure 26(b), was made as a simplified version of the previous model, containing only 1 strand rather than 3 that would be used to indicate just when the metal initially yielded. Since the first concept shown in Figure 26(a) was more complex, it was decided that the second concept would be tested instead to ease the manufacturing process.

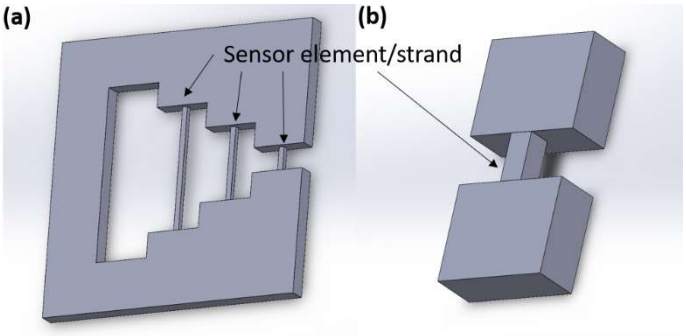


Figure 26. Conceptual designs of passive visual sensor. (a) Concept 1: this design has multiple strands to allow for measurement of multiple levels of strain. (b) Concept 2: this design contains only one strand meant to indicate only the yield strain.

The sensor dimensions were identified using numerical models. Using the concept 2 geometry, different variations were modelled in ANSYS. The ANSYS Static Structural module was used as it was the best fit for the problem because the loads involved in this problem have no significant damping or inertia effects and there are assumed to be steady loading and response conditions [44]. Analysis setup was a replica of what would be done during later tests. The interface between the sensor supports at the ends and the structure was defined by the bonded contact elements, which means that there were no gaps and no sliding [45]. The dimensions of the coupon are shown in Figure 27 and mesh specifications are shown in

Table X. These values were determined via trial and error. The mesh was automatically generated for the coupon and sensor and was refined at the gauge length and contact points using a sphere of influence and contact sizing, respectively. The sphere of influence allows the mesh to be refined within a user-defined sphere. Figure 28 shows the local coordinate system used for defining the center of the sphere of influence with respect to the global coordinate system for each geometry. Figure 29 shows the resulting mesh from the setup in Table X. A displacement was prescribed and was defined to reach its max at 0.5 seconds before returning to 0 at the end of the 1 second duration of the test. The displacement was assigned by trial and error to determine what was necessary to observe the yielding stress of the coupon as well as the ultimate stress in the sensor for each geometry variation. Initially, both the sensor and the coupon were defined to be made of steel. Material properties for steel are shown in Table XI.

Six different geometries of concept 2 were studied and two of them had desirable results. The geometries of these two variations are shown in Table XII and Figure 30 shows the description of each dimension. Other geometries were considered unfavorable due to the coupon yielding without the sensor reaching ultimate stress at all or reaching ultimate stress too late.

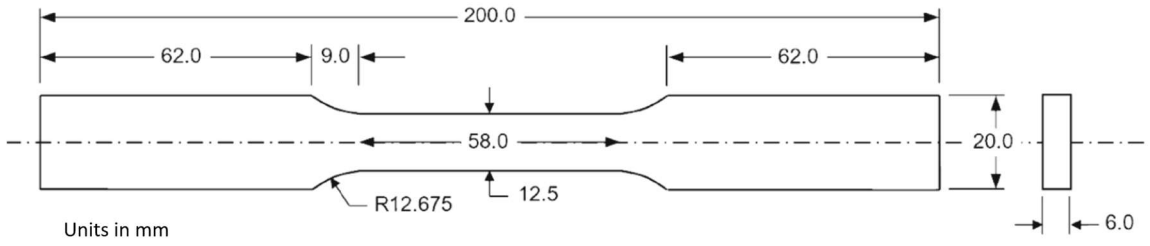


Figure 27. Dimensions of coupon.

Table X. SPECIFICATIONS OF FEM MESHING.

| | | |
|---|---|---|
| **Element Sizing:** | | |
| Element Sizing at Contact: | 0.3 | mm |
| Element Sizing Inside Sphere: | 0.8 | mm |
| Element Sizing Outside Sphere: | approx. 3-4 | mm |
| **Sphere of Influence Specifications:** | | |
| **Geometry 1** | | |
| Origin X: | -6.2E-07 | mm |
| Origin Y: | 6 | mm |
| Origin Z: | -100 | mm |
| Radius: | 29 | mm |
| **Geometry 2** | | |
| Origin X: | -6.2E-07 | mm |
| Origin Y: | 3 | mm |
| Origin Z: | -100 | mm |
| Radius: | 15 | mm |

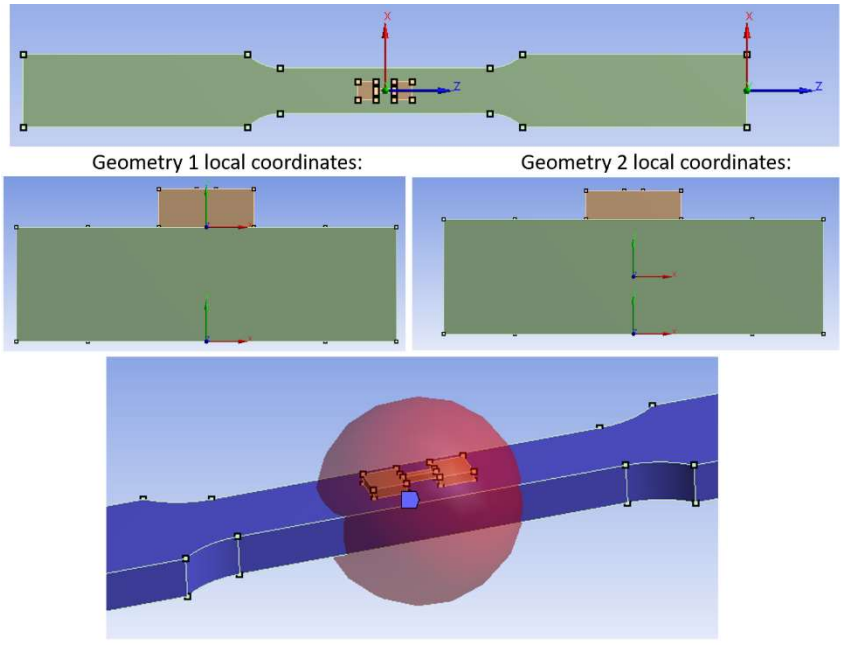


Figure 28. Detail of local coordinate system for sphere of influence.

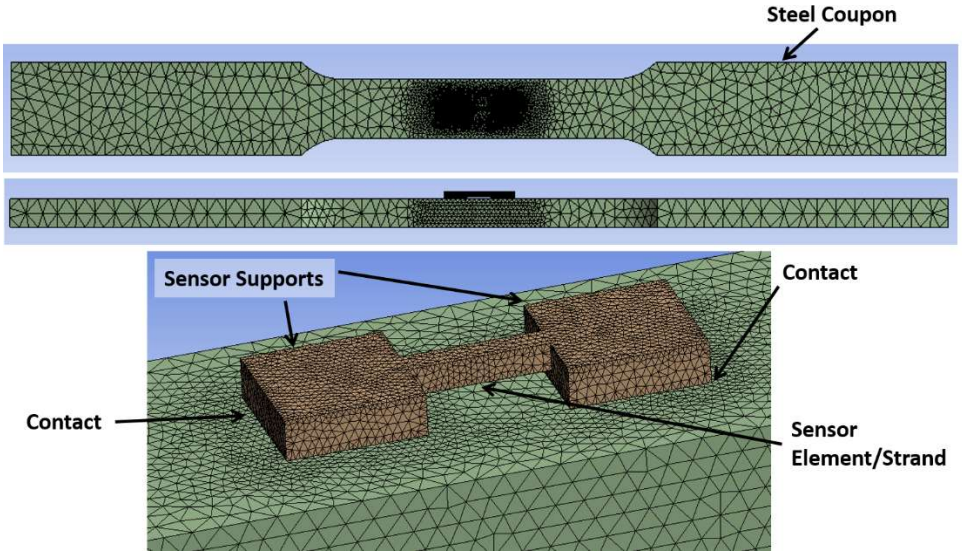


Figure 29. Meshed sensor and coupon geometry.

Table XI. MATERIAL PROPERTIES OF STEEL.

| Steel | | |
|---|---|---|
| Density | 7850 | kg/m$^3$ |
| Young's Modulus | 200000 | MPa |
| Poisson's Ratio | 0.3 | |
| Bulk Modulus | 166670 | MPa |
| Shear Modulus | 76923 | MPa |
| *Bilinear Isotropic Hardening* | | |
| Yield Strength | 345 | MPa |
| Tangent Modulus | 1450 | MPa |
| Tensile Ultimate Strength | 450 | MPa |

Table XII. GEOMETRIES OF THE TWO BEST PERFORMING VARIATIONS OF CONCEPT 2.

| **Geometry 1** | | | **Geometry 2** | | |
|---|---|---|---|---|---|
| $S_b$ | 5 | mm | $S_b$ | 5 | mm |
| $\boldsymbol{S_w}$ | **10** | **mm** | $\boldsymbol{S_w}$ | **15** | **mm** |
| $\boldsymbol{S_{end}}$ | **4** | **mm** | $\boldsymbol{S_{end}}$ | **5** | **mm** |
| $\boldsymbol{l_1}$ | **2** | **mm** | $\boldsymbol{l_1}$ | **5** | **mm** |
| $\boldsymbol{depth_s}$ | **2** | **mm** | $\boldsymbol{depth_s}$ | **1.5** | **mm** |
| $thick_{str}$ | 1 | mm | $thick_{str}$ | 1 | mm |
| $width_{str}$ | 1 | mm | $width_{str}$ | 1 | mm |

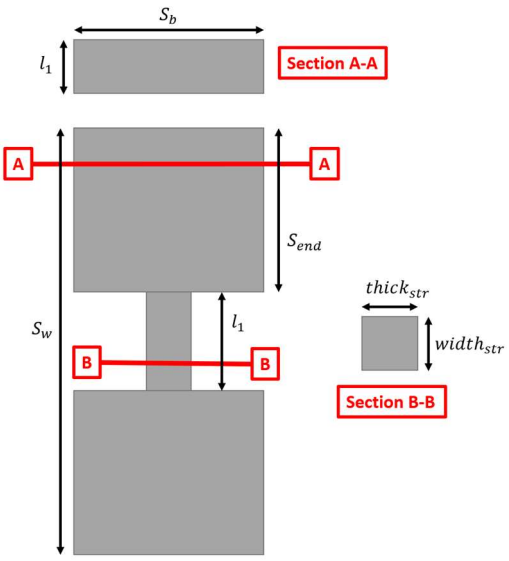


Figure 30. Definitions of dimensional variables used in Table XII.

In addition to metal as a sensor material, various polymers were also studied numerically as shown in Table XIII. Polystyrene, high impact polystyrene, acrylic, and VeroClear were modeled in ANSYS. Polystyrene, high impact polystyrene, and acrylic were chosen because of their brittleness and good durability to environmental factors such as temperature and humidity. VeroClear is an acrylic-like transparent photopolymer [46] that was also tested to be able to manufacture with 3D printing. Material properties for VeroClear were obtained from the PolyJet Materials Data Sheet [47].

Table XIII. MATERIAL PROPERTIES FOR PLASTICS TESTED DURING MODELLING.

| | Polystyrene | | High Impact Polystyrene | | Acrylic | | VeroClear | |
|---|---|---|---|---|---|---|---|---|
| Density | 1040 | kg/m$^3$ | 1040 | kg/m$^3$ | 1180 | kg/m$^3$ | 1190 | kg/m$^3$ |
| Young's Modulus | 2730 | MPa | 1720 | MPa | 2960 | MPa | 3000 | MPa |
| Poisson's Ratio | 0.395 | | 0.407 | | 0.395 | | 0.395 | |
| Bulk Modulus | 4333.3 | MPa | 3082.4 | MPa | 4269.8 | MPa | 4761.9 | MPa |
| Shear Modulus | 978.49 | MPa | 611.23 | MPa | 964.16 | MPa | 1075.3 | MPa |
| Yield Strength | 34.5 | MPa | 28 | MPa | 62.4 | MPa | 65 | MPa |
| Tensile Ultimate Strength | 43.1 | MPa | 29.2 | MPa | 67.1 | MPa | | |

In general, the results improved significantly using the chosen plastics as compared to steel. This allowed for the use of more discriminatory criteria in performance. To compare results, the reaction time was found. The reaction time is the time it takes for the sensor material to reach ultimate stress after the base coupon material, steel, reached yield stress. The equation for reaction time ($t_{reaction}$) is shown below:

$$t_{reaction} = t_{sensor\ @\ ultimate\ strain} - t_{base\ structure\ @\ yield\ strain} \quad (9)$$

The reaction time results for each model are summarized in Table XIV. The results of all the materials are shown in detail in Table XV to Table XIX, showing the prescribed displacement used and the maximum equivalent stress in the center of the top face of both the coupon and the sensor. Using steel, the two geometric variations with the best results did not reach ultimate stress exactly when the coupon yielded. This is indicated by the reaction time of 0.244 seconds for geometry 1 and 0.91 seconds for geometry 2 as shown in Table XIV. From Table XIV, the material that provided the shortest reaction time for both geometries was polystyrene. Therefore, the ideal sensor should be made from polystyrene as it had the fastest reaction time of 0.03 seconds for geometry 1 and 0.11 seconds for geometry 2. Although these were the ideal designs, due to available manufacturing methods and materials, the configurations experimentally tested were geometry 2 with acrylic and VeroClear as materials.

Table XIV. SUMMARY OF SENSOR REACTION TIMES.

| | **Reaction Times (s)** | |
|---|---|---|
| | **Geometry 1** | **Geometry 2** |
| **Steel** | 0.244 | 0.91 |
| **Polystyrene** | 0.03 | 0.11 |
| **Polystyrene, High Impact** | 0.05 | 0.11 |
| **Acrylic** | 0.08 | 0.24 |
| **VeroClear** | 0.08 | 0.25 |

Table XV. STRESS HISTORY FROM NUMERICAL MODELS USING STEEL WITH TWO GEOMETRIC DESIGNS OF CONCEPT 2.

**Coupon Material Properties:**

**Material:** Steel

**Yield Strength:** 345 MPa

**Tensile Ultimate Strength:** 450 MPa

**Sensor Material Properties:**

**Material:** Steel

**Yield Strength:** 345 MPa

**Tensile Ultimate Strength:** 450 MPa

**Geometry 1** **Displacement:** 10 mm

| Step | Time [s] | Increment [s] | *Coupon* [B] Equivalent Stress 2 (Max) [MPa] | *Sensor* [B] Equivalent Stress 5 (Max) [MPa] | |
|---|---|---|---|---|---|
| 0 | 0.0000 | --- | 0 | 0 | |
| 1 | 0.0125 | 0.0125 | 338.59 | 297.8 | |
| 2 | 0.0135 | 0.0010 | 336.98 | 235.3 | |
| 3 | 0.0145 | 0.0010 | 328.86 | 199.13 | |
| 4 | 0.0160 | 0.0015 | 323.77 | 166.69 | |
| 5 | 0.0183 | 0.0023 | 321.32 | 122.21 | |
| 6 | 0.0216 | 0.0034 | 332.15 | 66.548 | |
| 7 | **0.0267** | 0.0051 | **345.79** | 18.161 | |
| 8 | **0.0343** | 0.0076 | 347.51 | 33.255 | |
| 9 | **0.0457** | 0.0114 | 350.42 | 81.732 | |
| 10 | **0.0628** | 0.0171 | 355.55 | 100.39 | |
| 11 | **0.0884** | 0.0256 | 364.89 | 346.91 | |
| 12 | **0.1268** | 0.0384 | 383.45 | 372.31 | |
| 13 | **0.1845** | 0.0577 | 413.88 | 411.64 | **Reaction Time:** |
| 14 | **0.2710** | 0.0865 | 459.26 | **465.22** | **0.244** |
| 15 | 0.3794 | 0.1084 | 510.04 | 521.23 | |
| 16 | 0.5081 | 0.1287 | 558.34 | 572.78 | |
| 17 | 0.5148 | 0.0068 | 372.66 | 405.67 | |
| 18 | 0.5216 | 0.0067 | 191.37 | 238.92 | |
| 19 | 0.5317 | 0.0101 | 125.39 | 13.506 | |
| 20 | 0.5469 | 0.0152 | 529.58 | 383.42 | |
| 21 | 0.5492 | 0.0023 | 558.5 | 434.07 | |
| 22 | 0.5502 | 0.0010 | 558.75 | 465.83 | |
| 23 | 0.5512 | 0.0010 | 559.2 | 503.03 | |
| 24 | 0.5527 | 0.0015 | 560.97 | 551.41 | |
| 25 | 0.5550 | 0.0022 | 563.78 | 562.73 | |
| 26 | 0.5583 | 0.0034 | 565.53 | 573.29 | |
| 27 | 0.5634 | 0.0051 | 567.3 | 576.7 | |
| 28 | 0.5710 | 0.0076 | 569.95 | 581.31 | |
| 29 | 0.5824 | 0.0114 | 573.65 | 586.78 | |
| 30 | 0.5995 | 0.0171 | 576.91 | 589.49 | |
| 31 | 0.6251 | 0.0256 | 581.94 | 595.2 | |
| 32 | 0.6635 | 0.0384 | 589.89 | 604.33 | |
| 33 | 0.7212 | 0.0577 | 602.39 | 618.39 | |
| 34 | 0.8077 | 0.0865 | 621.66 | 639.43 | |
| 35 | 0.9375 | 0.1298 | 650.92 | 670.74 | |
| 36 | 1.0000 | 0.0626 | 665.05 | 685.69 | |

**Geometry 2** **Displacement:** 3 mm

| Step | Time [s] | Increment [s] | *Coupon* [B] Equivalent Stress 2 (Max) [MPa] | *Sensor* [B] Equivalent Stress 5 (Max) [MPa] | |
|---|---|---|---|---|---|
| 0 | 0.0000 | --- | 0 | 0 | |
| 1 | 0.0250 | 0.0250 | 191.78 | 216.24 | |
| 2 | 0.0363 | 0.0113 | 277.61 | 311.14 | |
| 3 | 0.0475 | 0.0113 | 305.96 | 278.69 | |
| 4 | 0.0526 | 0.0051 | 300.19 | 243.98 | |
| 5 | 0.0576 | 0.0051 | 298.87 | 212.67 | |
| 6 | 0.0652 | 0.0076 | 311.09 | 170.03 | |
| 7 | 0.0766 | 0.0114 | 342.98 | 117.69 | |
| 8 | **0.0937** | 0.0171 | **345.77** | 75.205 | |
| 9 | **0.1193** | 0.0256 | 347.35 | 63.438 | |
| 10 | **0.1578** | 0.0385 | 350.05 | 98.431 | |
| 11 | **0.2154** | 0.0577 | 355.16 | 346.41 | |
| 12 | **0.3019** | 0.0865 | 365.36 | 357.61 | |
| 13 | **0.4317** | 0.1298 | 382.22 | 378.42 | |
| 14 | **0.5193** | 0.0876 | 388.69 | 386.59 | |
| 15 | **0.5272** | 0.0080 | 327.32 | 317.36 | |
| 16 | **0.5352** | 0.0080 | 265.94 | 248.44 | |
| 17 | **0.5472** | 0.0120 | 173.89 | 144.95 | |
| 18 | **0.5651** | 0.0180 | 36.16 | 10.021 | |
| 19 | **0.5921** | 0.0269 | 171.97 | 233.48 | |
| 20 | **0.6325** | 0.0404 | 390.96 | 389.99 | |
| 21 | **0.6507** | 0.0182 | 393.26 | 393.72 | |
| 22 | **0.6688** | 0.0182 | 395.23 | 396.61 | |
| 23 | **0.6961** | 0.0273 | 398.41 | 401.1 | |
| 24 | **0.7370** | 0.0409 | 403.51 | 408.1 | |
| 25 | **0.7984** | 0.0614 | 411.43 | 418.8 | |
| 26 | **0.8904** | 0.0920 | 423.47 | 434.91 | **Reaction Time:** |
| 27 | **1.0000** | 0.1096 | 437.68 | **453.8** | **0.91** |

Table XVI. STRESS HISTORY FROM NUMERICAL MODELS USING POLYSTYRENE WITH TWO GEOMETRIC DESIGNS OF CONCEPT 2.

**Coupon Material Properties:**

**Material:** Steel

**Yield Strength:** 345 MPa

**Tensile Ultimate Strength:** 450 MPa

**Sensor Material Properties:**

**Material:** Polystyrene (PS)

**Yield Strength:** 34.5 MPa

**Tensile Ultimate Strength:** 43.1 MPa

**Geometry 1** **Displacement:** 10 mm

| Step | Time [s] | Increment [s] | *Coupon* [B] Equivalent Stress 2 (Max) [MPa] | *Sensor* [B] Equivalent Stress 5 (Max) [MPa] | |
|---|---|---|---|---|---|
| 0 | 0.0000 | --- | 0 | 0 | |
| 1 | 0.0125 | 0.0125 | 328.63 | 5.6064 | |
| 2 | **0.0150** | 0.0025 | **345.81** | 7.6045 | |
| 3 | **0.0176** | 0.0025 | 347.05 | 10.333 | |
| 4 | **0.0214** | 0.0038 | 348.89 | 14.301 | |
| 5 | **0.0271** | 0.0057 | 351.53 | 19.893 | |
| 6 | **0.0356** | 0.0085 | 355.38 | 27.818 | **Reaction Time:** |
| 7 | **0.0484** | 0.0128 | 360.99 | **38.995** | **0.03** |
| 8 | 0.0676 | 0.0192 | 369.26 | 54.766 | |
| 9 | 0.0965 | 0.0288 | 381.58 | 77.234 | |
| 10 | 0.1397 | 0.0433 | 399.96 | 109.3 | |
| 11 | 0.2046 | 0.0649 | 427.24 | 154.97 | |
| 12 | 0.3019 | 0.0973 | 466.68 | 218.47 | |
| 13 | 0.4479 | 0.1460 | 520.33 | 301.98 | |
| 14 | 0.4922 | 0.0443 | 535.89 | 325.97 | |
| 15 | 0.5122 | 0.0200 | 422.37 | 324.02 | |
| 16 | 0.5321 | 0.0200 | 125.76 | 315.05 | |
| 17 | 0.5456 | 0.0135 | 455.72 | 308.9 | |
| 18 | 0.5483 | 0.0027 | 536.05 | 303.11 | |
| 19 | 0.5493 | 0.0010 | 537.59 | 297.19 | |
| 20 | 0.5503 | 0.0010 | 539.24 | 291.01 | |
| 21 | 0.5518 | 0.0015 | 541.87 | 281.69 | |
| 22 | 0.5541 | 0.0023 | 545.82 | 268.27 | |
| 23 | 0.5574 | 0.0034 | 551.11 | 249.8 | |
| 24 | 0.5625 | 0.0051 | 557.45 | 226.37 | |
| 25 | 0.5701 | 0.0076 | 563.31 | 203 | |
| 26 | 0.5815 | 0.0114 | 568.45 | 183.19 | |
| 27 | 0.5986 | 0.0171 | 574.61 | 160.51 | |
| 28 | 0.6242 | 0.0256 | 580.37 | 140.57 | |
| 29 | 0.6626 | 0.0385 | 587.77 | 117.26 | |
| 30 | 0.7203 | 0.0577 | 597.82 | 88.945 | |
| 31 | 0.8068 | 0.0865 | 612.29 | 52.793 | |
| 32 | 0.9365 | 0.1298 | 633.97 | 4.7359 | |
| 33 | 1.0000 | 0.0635 | 644.64 | 17.973 | |

**Geometry 2** **Displacement:** 3 mm

| Step | Time [s] | Increment [s] | *Coupon* [B] Equivalent Stress 2 (Max) [MPa] | *Sensor* [B] Equivalent Stress 5 (Max) [MPa] | |
|---|---|---|---|---|---|
| 0 | 0.0000 | --- | 0 | 0 | |
| 1 | **0.0500** | 0.0500 | **345.78** | 7.541 | |
| 2 | **0.0551** | 0.0051 | 346.55 | 9.2343 | |
| 3 | **0.0601** | 0.0051 | 347.31 | 10.89 | |
| 4 | **0.0677** | 0.0076 | 348.42 | 13.312 | |
| 5 | **0.0791** | 0.0114 | 350.05 | 16.837 | |
| 6 | **0.0962** | 0.0171 | 352.41 | 21.913 | |
| 7 | **0.1218** | 0.0256 | 355.85 | 29.211 | **Reaction Time:** |
| 8 | **0.1603** | 0.0385 | 360.87 | **39.706** | **0.11** |
| 9 | 0.2179 | 0.0577 | 368.22 | 54.772 | |
| 10 | 0.3044 | 0.0865 | 379.05 | 76.642 | |
| 11 | 0.4342 | 0.1298 | 395.02 | 108.43 | |
| 12 | 0.5218 | 0.0876 | 400.36 | 119.03 | |
| 13 | 0.5415 | 0.0197 | 245.03 | 116.39 | |
| 14 | 0.5612 | 0.0197 | 89.709 | 113.74 | |
| 15 | 0.5907 | 0.0296 | 143.33 | 109.77 | |
| 16 | 0.6351 | 0.0443 | 405.93 | 89.786 | |
| 17 | 0.6550 | 0.0200 | 411.85 | 72.734 | |
| 18 | 0.6750 | 0.0200 | 415.13 | 63.539 | |
| 19 | 0.7049 | 0.0299 | 419.37 | 52.15 | |
| 20 | 0.7498 | 0.0449 | 425.14 | 37.451 | |
| 21 | 0.8171 | 0.0673 | 433.11 | 18.433 | |
| 22 | 0.9181 | 0.1010 | 444.42 | 6.8114 | |
| 23 | 1.0000 | 0.0819 | 453.33 | 26.024 | |

Table XVII. STRESS HISTORY FROM NUMERICAL MODELS USING HIGH IMPACT POLYSTYRENE WITH TWO GEOMETRIC DESIGNS OF CONCEPT 2.

**Coupon Material Properties:**

**Material:** Steel
**Yield Strength:** 345 MPa
**Tensile Ultimate Strength:** 450 MPa

**Sensor Material Properties:**

**Material:** High Impact Polystyrene
**Yield Strength:** 28 MPa
**Tensile Ultimate Strength:** 29.2 MPa

**Geometry 1** **Displacement:** 10 mm

| Step | Time [s] | Increment [s] | *Coupon* [B] Equivalent Stress 2 (Max) [MPa] | *Sensor* [B] Equivalent Stress 5 (Max) [MPa] | |
|---|---|---|---|---|---|
| 0 | 0.0000 | --- | 0 | 0 | |
| 1 | 0.0125 | 0.0125 | 328.34 | 3.5337 | |
| 2 | **0.0150** | 0.0025 | **345.9** | 4.9662 | |
| 3 | **0.0176** | 0.0025 | 347.19 | 6.7863 | |
| 4 | **0.0214** | 0.0038 | 349.09 | 9.453 | |
| 5 | **0.0271** | 0.0057 | 351.83 | 13.245 | |
| 6 | **0.0356** | 0.0085 | 355.82 | 18.671 | |
| 7 | **0.0484** | 0.0128 | 361.63 | 26.402 | **Reaction Time:** |
| 8 | **0.0676** | 0.0192 | 370.15 | **37.398** | **0.05** |
| 9 | 0.0965 | 0.0288 | 382.76 | 53.15 | |
| 10 | 0.1397 | 0.0433 | 401.41 | 75.702 | |
| 11 | 0.2046 | 0.0649 | 428.88 | 107.88 | |
| 12 | 0.3019 | 0.0973 | 468.37 | 152.77 | |
| 13 | 0.4479 | 0.1460 | 521.93 | 212.03 | |
| 14 | 0.5026 | 0.0547 | 539.26 | 231.05 | |
| 15 | 0.5137 | 0.0111 | 250.25 | 227.92 | |
| 16 | 0.5248 | 0.0111 | 67.673 | 224.78 | |
| 17 | 0.5414 | 0.0166 | 477.08 | 220.03 | |
| 18 | 0.5437 | 0.0023 | 539.34 | 217.57 | |
| 19 | 0.5447 | 0.0010 | 540.71 | 214.48 | |
| 20 | 0.5457 | 0.0010 | 542.34 | 210.98 | |
| 21 | 0.5472 | 0.0015 | 544.97 | 205.59 | |
| 22 | 0.5494 | 0.0022 | 548.82 | 197.88 | |
| 23 | 0.5528 | 0.0034 | 553.66 | 187.61 | |
| 24 | 0.5579 | 0.0051 | 558.89 | 175.38 | |
| 25 | 0.5655 | 0.0076 | 563.23 | 164.89 | |
| 26 | 0.5768 | 0.0114 | 567.93 | 154.08 | |
| 27 | 0.5939 | 0.0171 | 573.55 | 141.37 | |
| 28 | 0.6110 | 0.0171 | 577.36 | 133.17 | |
| 29 | 0.6366 | 0.0256 | 582.57 | 122.5 | |
| 30 | 0.6751 | 0.0384 | 589.64 | 109.01 | |
| 31 | 0.7328 | 0.0577 | 599.62 | 91.351 | |
| 32 | 0.8193 | 0.0865 | 614.19 | 67.674 | |
| 33 | 0.9490 | 0.1297 | 636.07 | 35.065 | |
| 34 | 1.0000 | 0.0510 | 644.71 | 22.559 | |

**Geometry 2** **Displacement:** 3 mm

| Step | Time [s] | Increment [s] | *Coupon* [B] Equivalent Stress 2 (Max) [MPa] | *Sensor* [B] Equivalent Stress 5 (Max) [MPa] | |
|---|---|---|---|---|---|
| 0 | 0.0000 | --- | 0 | 0 | |
| 1 | **0.0500** | 0.0500 | **345.87** | 4.9114 | |
| 2 | **0.0551** | 0.0051 | 346.66 | 6.0307 | |
| 3 | **0.0601** | 0.0051 | 347.44 | 7.1275 | |
| 4 | **0.0677** | 0.0076 | 348.59 | 8.7396 | |
| 5 | **0.0791** | 0.0114 | 350.28 | 11.092 | |
| 6 | **0.0962** | 0.0171 | 352.73 | 14.503 | |
| 7 | **0.1218** | 0.0256 | 356.3 | 19.43 | **Reaction Time:** |
| 8 | **0.1603** | 0.0385 | 361.51 | **26.55** | **0.11** |
| 9 | 0.2179 | 0.0577 | 369.11 | 36.804 | |
| 10 | 0.3044 | 0.0865 | 380.29 | 51.696 | |
| 11 | 0.4342 | 0.1298 | 396.71 | 73.313 | |
| 12 | 0.5218 | 0.0876 | 402.19 | 80.514 | |
| 13 | 0.5395 | 0.0177 | 262.4 | 79.013 | |
| 14 | 0.5572 | 0.0177 | 122.62 | 77.511 | |
| 15 | 0.5838 | 0.0266 | 87.091 | 75.259 | |
| 16 | 0.6237 | 0.0399 | 394.86 | 71.942 | |
| 17 | 0.6417 | 0.0180 | 408.95 | 60.086 | |
| 18 | 0.6596 | 0.0180 | 412.4 | 53.979 | |
| 19 | 0.6866 | 0.0269 | 416.39 | 47.276 | |
| 20 | 0.7270 | 0.0404 | 421.82 | 38.469 | |
| 21 | 0.7876 | 0.0606 | 429.38 | 26.826 | |
| 22 | 0.8785 | 0.0909 | 440.04 | 11.193 | |
| 23 | 1.0000 | 0.1215 | 453.79 | 8.1496 | |

Table XVIII. STRESS HISTORY FROM NUMERICAL MODELS USING ACRYLIC WITH TWO GEOMETRIC DESIGNS OF CONCEPT 2.

**Coupon Material Properties:**

**Material:** Steel

**Yield Strength:** 345 MPa

**Tensile Ultimate Strength:** 450 MPa

**Sensor Material Properties:**

**Material:** Acrylic (PMMA)

**Yield Strength:** 62.4 MPa

**Tensile Ultimate Strength:** 67.1 MPa

**Geometry 1** **Displacement:** 10 mm

| Step | Time [s] | Increment [s] | *Coupon* [B] Equivalent Stress 2 (Max) [MPa] | *Sensor* [B] Equivalent Stress 5 (Max) [MPa] | |
|---|---|---|---|---|---|
| 0 | 0.0000 | --- | 0 | 0 | |
| 1 | 0.0125 | 0.0125 | 328.62 | 5.5246 | |
| 2 | **0.0150** | 0.0025 | **345.81** | 7.5042 | |
| 3 | **0.0176** | 0.0025 | 347.06 | 10.199 | |
| 4 | **0.0214** | 0.0038 | 348.9 | 14.119 | |
| 5 | **0.0271** | 0.0057 | 351.54 | 19.644 | |
| 6 | **0.0356** | 0.0085 | 355.39 | 27.478 | |
| 7 | **0.0484** | 0.0128 | 361.01 | 38.531 | |
| 8 | **0.0676** | 0.0192 | 369.29 | 54.132 | **Reaction Time:** |
| 9 | **0.0965** | 0.0288 | 381.62 | **76.361** | **0.08** |
| 10 | 0.1397 | 0.0433 | 400.02 | 108.09 | |
| 11 | 0.2046 | 0.0649 | 427.31 | 153.28 | |
| 12 | 0.3019 | 0.0973 | 466.75 | 216.11 | |
| 13 | 0.4479 | 0.1460 | 520.4 | 298.78 | |
| 14 | 0.4971 | 0.0493 | 537.68 | 325.1 | |
| 15 | 0.5082 | 0.0111 | 398.52 | 322.74 | |
| 16 | 0.5193 | 0.0111 | 120.08 | 317.83 | |
| 17 | 0.5359 | 0.0166 | 342.56 | 310.47 | |
| 18 | 0.5410 | 0.0051 | 460.19 | 308.1 | |
| 19 | 0.5432 | 0.0023 | 535.12 | 303.77 | |
| 20 | 0.5455 | 0.0023 | 541.15 | 290.33 | |
| 21 | 0.5478 | 0.0023 | 545.18 | 276.49 | |
| 22 | 0.5512 | 0.0034 | 550.88 | 257.23 | |
| 23 | 0.5563 | 0.0051 | 557.82 | 232.49 | |
| 24 | 0.5640 | 0.0077 | 564.42 | 206.77 | |
| 25 | 0.5755 | 0.0115 | 569.84 | 186.04 | |
| 26 | 0.5927 | 0.0173 | 575.88 | 163.8 | |
| 27 | 0.6186 | 0.0259 | 581.51 | 144.5 | |
| 28 | 0.6575 | 0.0388 | 588.99 | 121.04 | |
| 29 | 0.7157 | 0.0582 | 599.17 | 92.518 | |
| 30 | 0.8031 | 0.0874 | 613.78 | 56.217 | |
| 31 | 0.9341 | 0.1311 | 635.66 | 8.0577 | |
| 32 | 1.0000 | 0.0659 | 646.73 | 15.247 | |

**Geometry 2** **Displacement:** 3 mm

| Step | Time [s] | Increment [s] | *Coupon* [B] Equivalent Stress 2 (Max) [MPa] | *Sensor* [B] Equivalent Stress 5 (Max) [MPa] | |
|---|---|---|---|---|---|
| 0 | 0.0000 | --- | 0 | 0 | |
| 1 | **0.0500** | 0.0500 | **345.79** | 7.4401 | |
| 2 | **0.0551** | 0.0051 | 346.56 | 9.1118 | |
| 3 | **0.0601** | 0.0051 | 347.31 | 10.746 | |
| 4 | **0.0677** | 0.0076 | 348.42 | 13.138 | |
| 5 | **0.0791** | 0.0114 | 350.05 | 16.619 | |
| 6 | **0.0962** | 0.0171 | 352.42 | 21.633 | |
| 7 | **0.1218** | 0.0256 | 355.87 | 28.844 | |
| 8 | **0.1603** | 0.0385 | 360.9 | 39.214 | |
| 9 | **0.2179** | 0.0577 | 368.25 | 54.102 | **Reaction Time:** |
| 10 | **0.3044** | 0.0865 | 379.1 | **75.716** | **0.24** |
| 11 | 0.4342 | 0.1298 | 395.09 | 107.13 | |
| 12 | 0.5218 | 0.0876 | 400.43 | 117.61 | |
| 13 | 0.5415 | 0.0197 | 245.1 | 115 | |
| 14 | 0.5612 | 0.0197 | 89.778 | 112.39 | |
| 15 | 0.5907 | 0.0296 | 143.26 | 108.48 | |
| 16 | 0.6351 | 0.0443 | 405.98 | 88.851 | |
| 17 | 0.6550 | 0.0200 | 411.86 | 72.167 | |
| 18 | 0.6750 | 0.0200 | 415.12 | 63.157 | |
| 19 | 0.7049 | 0.0299 | 419.36 | 51.941 | |
| 20 | 0.7498 | 0.0449 | 425.13 | 37.454 | |
| 21 | 0.8171 | 0.0673 | 433.11 | 18.691 | |
| 22 | 0.9181 | 0.1010 | 444.43 | 6.2372 | |
| 23 | 1.0000 | 0.0819 | 453.36 | 25.215 | |

Table XIX. STRESS HISTORY FROM NUMERICAL MODELS USING VEROCLEAR WITH TWO GEOMETRIC DESIGNS OF CONCEPT 2.

**Coupon Material Properties:**
**Material:** Steel
**Yield Strength:** 345 MPa
**Tensile Ultimate Strength:** 450 MPa

**Sensor Material Properties:**
**Material:** VeroClear
**Yield Strength:** 65 MPa

**Geometry 1** **Displacement:** 10 mm

| Step | Time [s] | Increment [s] | *Coupon* [B] Equivalent Stress 2 (Max) [MPa] | *Sensor* [B] Equivalent Stress 5 (Max) [MPa] | |
|---|---|---|---|---|---|
| 0 | 0.0000 | --- | 0 | 0 | |
| 1 | 0.0125 | 0.0125 | 328.71 | 6.1579 | |
| 2 | **0.0150** | 0.0025 | **345.78** | 8.2769 | |
| 3 | **0.0176** | 0.0025 | 347.02 | 11.23 | |
| 4 | **0.0214** | 0.0038 | 348.84 | 15.517 | |
| 5 | **0.0271** | 0.0057 | 351.46 | 21.545 | |
| 6 | **0.0356** | 0.0085 | 355.27 | 30.066 | |
| 7 | **0.0484** | 0.0128 | 360.83 | 42.058 | |
| 8 | **0.0676** | 0.0192 | 369.04 | 58.947 | **Reaction Time:** |
| 9 | **0.0965** | 0.0288 | 381.29 | **82.979** | **0.08** |
| 10 | 0.1397 | 0.0433 | 399.6 | 117.26 | |
| 11 | 0.2046 | 0.0649 | 426.82 | 166.06 | |
| 12 | 0.3019 | 0.0973 | 466.2 | 233.87 | |
| 13 | 0.4479 | 0.1460 | 519.81 | 322.97 | |
| 14 | 0.5026 | 0.0547 | 537.16 | 351.48 | |
| 15 | 0.5137 | 0.0111 | 250.27 | 346.01 | |
| 16 | 0.5248 | 0.0111 | 85.146 | 340.54 | |
| 17 | 0.5414 | 0.0166 | 468.33 | 331.81 | |
| 18 | 0.5437 | 0.0023 | 538.18 | 322.2 | |
| 19 | 0.5459 | 0.0023 | 542.05 | 306.34 | |
| 20 | 0.5494 | 0.0034 | 548.08 | 283.44 | |
| 21 | 0.5545 | 0.0051 | 555.78 | 253.41 | |
| 22 | 0.5621 | 0.0077 | 563.75 | 219.61 | |
| 23 | 0.5736 | 0.0115 | 569.7 | 193.75 | |
| 24 | 0.5909 | 0.0173 | 575.97 | 167.92 | |
| 25 | 0.6168 | 0.0259 | 581.69 | 145.88 | |
| 26 | 0.6556 | 0.0388 | 589.21 | 119.58 | |
| 27 | 0.7139 | 0.0582 | 599.42 | 87.902 | |
| 28 | 0.8012 | 0.0874 | 614.05 | 48.002 | |
| 29 | 0.9323 | 0.1311 | 635.94 | 4.6724 | |
| 30 | 1.0000 | 0.0677 | 647.33 | 30.559 | |

**Geometry 2** **Displacement:** 3 mm

| Step | Time [s] | Increment [s] | *Coupon* [B] Equivalent Stress 2 (Max) [MPa] | *Sensor* [B] Equivalent Stress 5 (Max) [MPa] | |
|---|---|---|---|---|---|
| 0 | 0.0000 | --- | 0 | 0 | |
| 1 | **0.0500** | 0.0500 | **345.76** | 8.2163 | |
| 2 | **0.0551** | 0.0051 | 346.52 | 10.052 | |
| 3 | **0.0601** | 0.0051 | 347.27 | 11.849 | |
| 4 | **0.0677** | 0.0076 | 348.37 | 14.472 | |
| 5 | **0.0791** | 0.0114 | 349.99 | 18.289 | |
| 6 | **0.0962** | 0.0171 | 352.33 | 23.774 | |
| 7 | **0.1218** | 0.0256 | 355.74 | 31.653 | |
| 8 | **0.1603** | 0.0385 | 360.72 | 42.971 | |
| 9 | **0.2179** | 0.0577 | 368 | 59.207 | **Reaction Time:** |
| 10 | **0.3044** | 0.0865 | 378.75 | **82.775** | **0.25** |
| 11 | 0.4342 | 0.1298 | 394.61 | 117.05 | |
| 12 | 0.5218 | 0.0876 | 399.91 | 128.48 | |
| 13 | 0.5415 | 0.0197 | 244.57 | 125.57 | |
| 14 | 0.5612 | 0.0197 | 89.251 | 122.67 | |
| 15 | 0.5907 | 0.0296 | 143.8 | 118.3 | |
| 16 | 0.6351 | 0.0443 | 405.61 | 95.886 | |
| 17 | 0.6550 | 0.0200 | 411.79 | 76.314 | |
| 18 | 0.6750 | 0.0200 | 415.13 | 65.939 | |
| 19 | 0.7049 | 0.0299 | 419.39 | 53.311 | |
| 20 | 0.7498 | 0.0449 | 425.15 | 37.177 | |
| 21 | 0.8171 | 0.0673 | 433.08 | 16.457 | |
| 22 | 0.9181 | 0.1010 | 444.31 | 10.892 | |
| 23 | 1.0000 | 0.0819 | 453.16 | 31.657 | |

## 4.3 Experimental Results

Due to the miniature and fragile sensor geometry, 3D printing was chosen initially as the manufacturing method. The sensor was printed out of VeroClear using the Objet30 Prime 3D printer and spray painted to enhance visibility during testing as shown in Figure 31(a). To adhere the sensor to the coupon, Loctite® E-120hp adhesive was used. Loctite® E-120hp adhesive is an industrial grade epoxy adhesive that was chosen because it was the strongest structural adhesive in lap shear strength available to be obtained for this experiment that also had resistance to harsh environments involving rapid temperature

changes and exposure to acetone, fuel and oil [48]. Resistance to harsh environments is important because the setup would need to be exposed to real world conditions for its intended use. According to the technical data sheet for Loctite® E-120hp, the adhesive's lap shear strength on stainless steel is 23.44 MPa [49]. After applying it to the sensor and coupon, they were left to cure overnight to ensure that the bonds were at full strength. The coupon was made from A572 grade 50 steel.

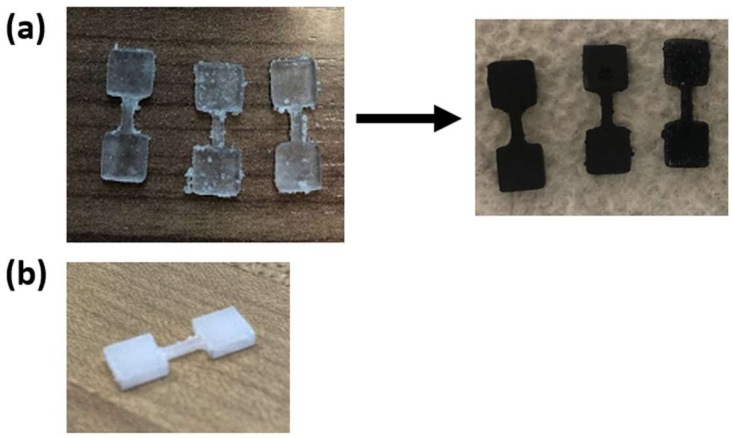


Figure 31. Manufactured sensors, (a) 3D printed sensors made from VeroClear were spray painted for visibility and (b) sensors milled from a sheet of opaque white acrylic.

The first experimental setup is shown in Figure 32. The purpose of this test was to determine if the concept of using the sensor for detecting localized defects would be viable. Two sensors were attached to the coupon, one in the gauge length and one outside the gauge length. The sensor attached outside of the gauge length was to be used as a control. The bonded coupon and sensors were rigged to the model 1125 MTS tensile machine and the coupon was loaded at 2 mm/min until it passed yielding. The result from this experimental trial is shown in Figure 33. The sensor in the gauge length failed via shear at the bottom end when the coupon reached yielding, which was not the desired failure mode. This result was thought to be due to the fact that the sensor was 3D printed, as the layers

may have caused the part to be weaker in the plane of the shear failure and possibly due to a defect during manufacturing or both. The sensor outside of the gauge length was unaffected, which shows that the concept is viable. More work is needed in order to fine tune the strand to break at the exact moment of yielding but this was not the focus of these experiments. Rather, these trials are focused on the initial problem of adhering the sensor to the coupon and determining the failure modes of the sensor in experimental conditions.

Figure 32. Experimental setup for the first coupon.


Figure 33. Results from the first experiment. The sensor at the gauge area failed due to shear at one of the ends instead of breaking at the middle. The other sensor outside the gauge area remained unchanged which validates the concept.

For the next trials, it was decided that to avoid the shear failure from the previous trial, the sensor should be manufactured from a solid sheet of material instead. Using CNC milling, sensors were able to be manufactured from a sheet of opaque, white acrylic. Since the material was opaque, there was no need to spray paint the part for visibility. This time, just one sensor was bonded to the coupon and the experiment was focused on achieving the desired failure mode as shown in Figure 34. This was that the sensor would break at the strand to indicate that the coupon has yielded. To observe the sensor's behavior more closely, an optical microscope was set up to capture footage of the failure as it happened. After running the tensile test, the results were as shown in Figure 35. The sensor did not break, but instead the adhesive bond failed. Two trials were done using the milled sensors with the same result. This means that a better method of attaching the sensor to the coupon is needed in order for the concept to work. In numerical models, the contact was assumed to be perfect and did not account for the properties of an adhesive or shifting like what was seen during footage of the experiment using the optical microscope. The shifting sensor is shown in Figure 36. For the concept to work, a stronger adhesive or another method of attachment would be needed. Ideally, the connection between the sensor and the coupon would need to have a shear strength greater than 345 MPa, the yielding strength of the A572 grade 50 steel, for the sensor to behave more similarly to the numerical model since it assumed a perfect bond.

Figure 34. Experimental setup for the second and third coupons.

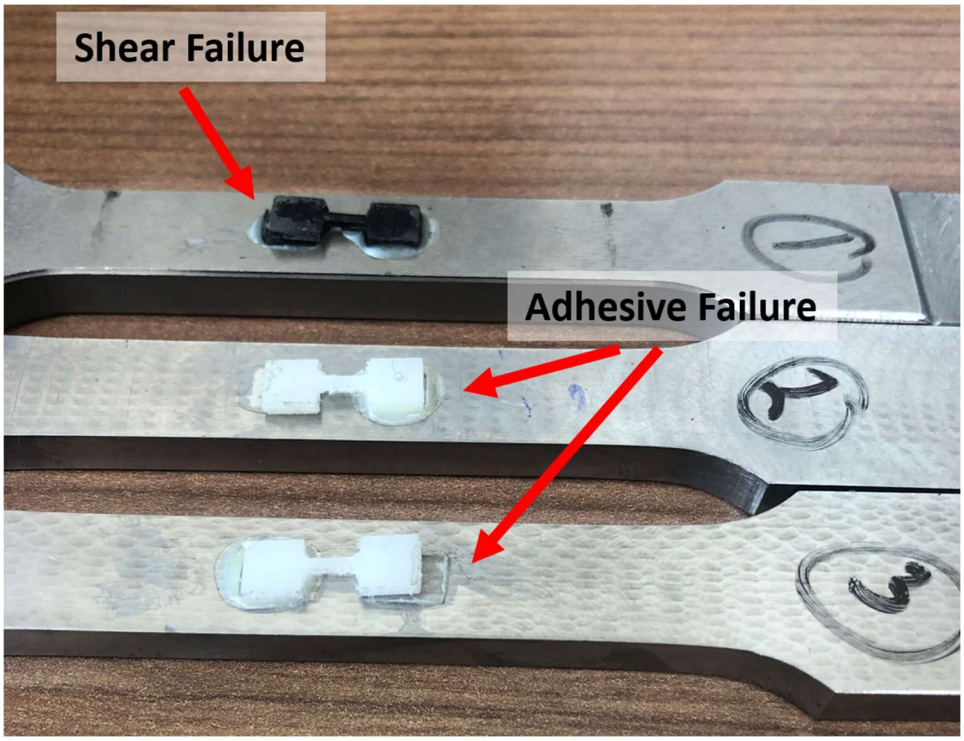


Figure 35. Showing all failure modes of sensors from the three experiments. The sensors at the second and third coupons did not break since the adhesive failed instead.

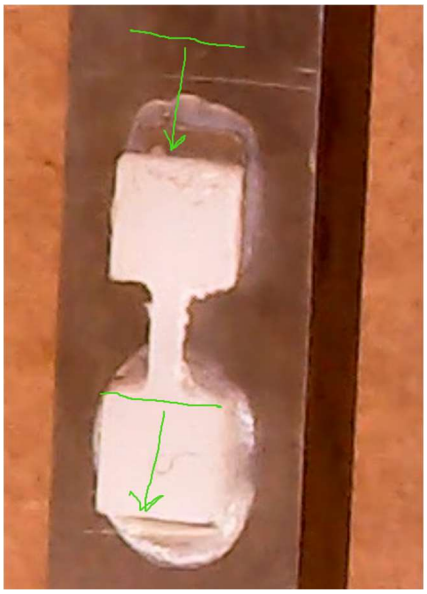

Figure 36. Sensor shifting during tensile test. Drawn lines indicate the position of the top and bottom of the sensor at the start of the experiment.

# 5. CONCLUSIONS AND FUTURE WORK

## 5.1 Summary

UAVs offer bridge inspectors a powerful tool to perform their job more quickly, cost-effectively, and safely. They can provide data for digital life cycle monitoring of structures as well as a new perspective. 3D models created from UAV captured images can allow inspectors to evaluate structures in house, but for this to be possible the model needs to be highly accurate geometrically and texture wise. In this thesis, data collected from the DJI Phantom 4 Pro drone was processed through 2D and 3D image analyses. For 3D reconstruction, a path plan was developed to efficiently gather the images required to create an accurate and successful 3D reconstructed model using ContextCapture. The passive visual sensor developed in this thesis was intended to allow for non-visual plastic deformations to be detected through visual inspection. By having the sensor element rupture when the base material reaches yield strain, the non-visual plastic deformation can be indirectly detected.

## 5.2 Findings

3D model findings were divided qualitatively and quantitatively. Qualitative results showed that using multiple camera angles and elevations helped the most in reducing the number of holes and distortions. It is important to get closer to the subject and to focus on providing more views of the vulnerable areas. In this case it was the underside of the top flange due to the shadow effect. For improving texture, pictures taken up close for all surfaces of the girder were what mattered most. Trends also suggested that texture improved when there were low model distortions. Quantitative results showed that overall accuracy depended on reference point quality. Data collection during experiments primarily focused on improving the girder geometry qualitatively in terms of shadow effect distortion but did not focus on calibration sheet quality which had a big impact on overall accuracy due to the calibration sheet's role in creating a conversion factor between actual units and the arbitrary units from the model. Therefore, when collecting data for 3D reconstruction, reference points for unit conversions need to be properly

accounted for. Results for accuracy by measurement were dependent on the model distortion trends and tended to involve problems with the web and flange.

The proposed methodology presented in this study provides effective guidelines that have potential to provide higher accuracy girder models with fewer photos. Results showed that the methodology was able to produce a model with the highest accuracy of all models with less than 332 pictures. More testing is needed to finalize the guidelines as there are limitations for it regarding web and flange depths. For larger web or flange depths, the proposed methodology may not provide sufficient overlap between images. Improvements may involve adding additional corner views or including additional positions depending on depth or width.

For analyzing the 2D images to identify localized defects, exposing the area of interest to direct light improves the measurement consistency because it helps to avoid jagged edges. Another finding was that larger lengths on the scale of 90 mm could be measured with a percent error of only 0-3% while measuring smaller ones on the scale of 2 mm had a percent error of 10-30%. More testing is needed to determine the minimum length of measurement that can be extracted from a 2D image from a DJI Phantom 4 Pro UAV with satisfactory accuracy.

Both processing methods depend on good image quality and, while this study only focused on using the DJI Phantom 4 Pro's camera, in future works other cameras could be tested to see the impact of different camera qualities on 2D and 3D processing. A limitation of the experiment was that the DJI Phantom 4 Pro cannot rotate its camera above the horizontal, so while it worked with the girder positioned below it, under more realistic circumstances with the girders positioned above it, this UAV would not be able to collect the images as proposed by the methodology and otherwise. Ideally, the UAV should likely have a top mounted camera or a gimbal that allows for an upward view for proper execution of this methodology under more realistic conditions. Another limitation to the experiment due to the girder being placed on the

ground rather than on a ceiling is that there is much more light available than there would be under a bridge, which would impact image quality.

Although it was already an industrial strength adhesive, Loctite® E-120hp was not able to provide the strength needed to allow the sensor to behave as it was intended. Results showed that the concept is viable but the execution needs to be improved. It was found that the sensor needs to have a better method of attachment to the base material for it to behave as intended. During experimental trials, the adhesive used failed before the sensor. It was also found that milling the sensor worked better than 3D printing it since the 3D printed sensor failed due to shear at the sensor supports likely due to manufacturing defect or due to being manufactured in layers.

### 5.3 Future Works

Future works for 3D processing include performing additional trials of the methodology with greater overlap to confirm trends, using models created using the methodology and testing accuracy for smaller defects such as what was done in this thesis for 2D images, and testing the methodology in a more realistic setup with the girder suspended and confined. This would require the use of a different UAV than the DJI Phantom 4 Pro. Different web depths and flange depths should be tested and the methodology should be refined to accommodate them. Applying image enhancement to images prior to creating a 3D model should also be explored. For 2D processing, future works include using more realistic defects rather than a calibration sheet, which made measurement easier due to the high contrast, and performing a more thorough experiment testing the accuracy of defect measurements at incremental lengths between 90 mm and 2 mm. Additionally, more image processing masks and techniques should be tested using the realistic defects. As proper lighting is important for both 2D and 3D tasks, the development of an effective, cost effective, and portable method for lighting the underside of bridges for UAV image acquisition would be valuable to allow UAVs to capture more quality

images. For 3D reconstruction, the light cannot be carried with the UAV, which is the challenge. For the passive sensor, different attachment methods should be developed that will secure the sensor to the base material without failing before the sensor strand does. The sensors may also require a different design for this to be possible.

# 6. APPENDIX

Methodology calculations worked out:

$$FOV = \frac{fres * imres}{fpix * 1000\,\frac{mm}{m}} = \frac{2\,mm * 3078\,px}{4\,px * 1000\,\frac{mm}{m}} = 1.54\,m \tag{1}$$

$$wkdt = \frac{FOV}{2 * \tan\left(\frac{\alpha}{2}\right)} = \frac{1.54\,m}{2 * \tan\left(\frac{84°}{2}\right)} = 0.855\,m \tag{2}$$

$$lap = user_{pctlap} * FOV = 0.7 * 1.54\,m = 1.08\,m$$

$$\downarrow$$

$$hlap = \frac{lap}{2} = \frac{1.08}{2} = 0.539\,m \tag{3}$$

$$x1 = \frac{hlap}{\tan\left(\frac{\alpha}{2}\right)} = \frac{0.539}{\tan\left(\frac{84°}{2}\right)} = 0.598\,m$$

$$x2 = wkdt - x1 = 0.855\,m - 0.598\,m = 0.256\,m$$

$$\Delta\lambda = 2 * x2 * \tan\left(\frac{\alpha}{2}\right) = 2 * 0.256\,m * \tan\left(\frac{84°}{2}\right) = 0.462\,m \tag{4}$$

From Table II:

$$SidePosV = \frac{D}{2} + H = \frac{1.75\,m}{2} + 0.0884\,m = 0.963\,m$$

$$SidePosH = wkdt - \frac{W}{2} = 0.855\,m - \frac{0.509\,m}{2} = 0.6\,m$$

$$A1S = \tan^{-1}\left(\frac{\frac{D}{2}}{wkdt}\right) = \tan^{-1}\left(\frac{\frac{1.75\,m}{2}}{0.855\,m}\right) = 45.68°$$

$$A2S = 0°$$

$$A3S = -\tan^{-1}\left(\frac{\frac{D}{2}}{wkdt}\right) = -\tan^{-1}\left(\frac{\frac{1.75\ m}{2}}{0.855\ m}\right) = -45.68°$$

$$CorPosV = D + H + wkdt * \sin(15°) = 1.75\ m + 0.0884\ m + 0.855\ m * \sin(15°) = 2.06\ m$$

$$CorPosH = wkdt * \cos(15°) = 0.855\ m * \cos(15°) = 0.825\ m$$

$$A1C = 15°$$

$$BotPosV = wkdt + D + H = 0.855\ m + 1.75\ m + 0.0884\ m = 2.69\ m$$

$$BotPosH = -\frac{W}{2} = -\frac{0.509\ m}{2} = -0.255\ m$$

$$A1B = \tan^{-1}\left(\frac{\frac{W}{2}}{wkdt}\right) + 90° = \tan^{-1}\left(\frac{\frac{0.509\ m}{2}}{0.855\ m}\right) + 90° = 106.61°$$

$$A2B = 90°$$

$$A3B = 90° - \tan^{-1}\left(\frac{\frac{W}{2}}{wkdt}\right) = 90° - \tan^{-1}\left(\frac{\frac{0.509\ m}{2}}{0.855\ m}\right) = 73.39°$$

$$numVPI = \frac{L}{\Delta\lambda} * 5 * G_N = \frac{42.7\ m}{0.462\ m} * 5 * 4 = 1849.69 \approx 1850\ VPIs \quad (5)$$

$$numPics = \left(\frac{L}{\Delta\lambda} * 3 * 2 + \frac{L}{\Delta\lambda} * 1 * 2 + \frac{L}{\Delta\lambda} * 3 * 1\right) * G_N$$

$$= \left(\frac{42.7\ m}{0.462\ m} * 3 * 2 + \frac{42.7\ m}{0.462\ m} * 1 * 2 + \frac{42.7\ m}{0.462\ m} * 3 * 1\right) * 4 \quad (6)$$

$$= 4069.31 \approx 4069\ photos$$

$$betV1 = CorPosV - SidePosV = 2.06\ m - 0.963\ m = 1.10\ m$$

$$betH1 = CorPosH - SidePosH = 0.825\ m - 0.6\ m = 0.226\ m$$

$$betV2 = BotPosV - CorPosV = 2.69\ m - 2.06\ m = 0.633\ m$$

$$betH2 = CorPosH - BotPosH = 0.825\ m - (-0.255\ m) = 1.08\ m$$

$$betGirders = abs(S - SidePosH * 2) = abs(3.66\ m - 0.6\ m * 2) = 2.46\ m$$

$$travelDistance = G_N * 5 * L + 2 * (betV1 + betH1 + betV2 + betH2) + (G_N - 1) * betGirders \quad (7)$$
$$= 4 * 5 * 42.7\ m + 2 * (1.096 + 0.226 + 0.633 + 1.08) + (4 - 1) * 2.46\ m = 867.45\ m$$

$$travelTime = \frac{travelDistance}{speed * 1000 \frac{m}{km} * \frac{1\ hr}{3600\ s}} + numPics * captureTime \quad (8)$$
$$= \frac{867.45\ m}{0.805\ kph * 1000 \frac{m}{km} * \frac{1\ hr}{3600\ s}} + 4069.31 * 1\ s = 7948.61\ s$$
$$\rightarrow 132.48\ min$$

# 7. CITED LITERATURE


1. American Association of State Highway and Transportation Officials. *AASHTO Bridge Element Inspection Guide Manual.* , 2010.

2. Chen, Siyuan, et al. "UAV Bridge Inspection through Evaluated 3D Reconstructions." *Journal of Bridge Engineering*, vol. 24, no. 4, 2019, pp. 5019001. *CrossRef*, http://ascelibrary.org/doi/abs/10.1061/(ASCE)BE.1943-5592.0001343, doi:10.1061/(ASCE)BE.1943-5592.0001343.

3. Hubbard, Bryan, and Sarah Hubbard. "Unmanned Aircraft Systems (UAS) for Bridge Inspection Safety." *Drones (Basel)*, vol. 4, no. 3, 2020. *CrossRef*, https://doaj.org/article/140fc1fa25a84631a76c44b55db2e291, doi:10.3390/drones4030040.

4. Popescu, Cosmin, et al. *Bridge Inspections using Unmanned Aerial Vehicles – A Case Study in Sweden.* , 2021.

5. Federal Highway Administration. *National Bridge Inspection Standards.* , 2004.

6. American Association of State Highway and Transportation Officials. *Manual for Condition Evaluation of Bridges.* , 1994.

7. Federal Highway Administration. *Bridge Inspector's Reference Manual.* , 2012.

8. ASTM E1316-21. *Standard Terminology for Nondestructive Examinations.* , 2021.

9. Kocer, Basaran B., et al. "Inspection-while-Flying: An Autonomous Contact-Based Nondestructive Test using UAV-Tools." *Automation in Construction*, vol. 106, 2019, pp. 102895. *CrossRef*, https://dx.doi.org/10.1016/j.autcon.2019.102895, doi:10.1016/j.autcon.2019.102895.

10. Papaelias Mayorkinos, Márquez Fausto Pedro García, and Karyotakis Alexander. "A Review on Condition Monitoring System for Solar Plants Based on Thermography." *Non-Destructive Testing and Condition Monitoring Techniques for Renewable Energy Industrial Assets.* Elsevier, 2020.

11. Bin Yang, et al. *Non-Destructive Testing of Wind Turbine Blades using an Infrared Thermography: A Review*, vol. 1, IEEE, Aug 2013.

12. Lerma, José L., Miriam Cabrelles, and Cristina Portalés. "Multitemporal Thermal Analysis to Detect Moisture on a Building Façade." *Construction & Building Materials*, vol. 25, no. 5, 2011, pp. 2190-2197. *CrossRef*, https://dx.doi.org/10.1016/j.conbuildmat.2010.10.007, doi:10.1016/j.conbuildmat.2010.10.007.

13. Kromanis, Rolands, and Christopher Forbes. "A Low-Cost Robotic Camera System for Accurate Collection of Structural Response." *Inventions (Basel)*, vol. 4, no. 3, 2019, pp. 47. *CrossRef*, https://explore.openaire.eu/search/publication?articleId=dedup_wf_001::9908ff180854e3b2991a2be037469abb, doi:10.3390/inventions4030047..

14. Greenwood, William W., Jerome P. Lynch, and Dimitrios Zekkos. "Applications of UAVs in Civil Infrastructure." *Journal of Infrastructure Systems*, vol. 25, no. 2, 2019, pp. 4019002. *CrossRef*, http://ascelibrary.org/doi/abs/10.1061/(ASCE)IS.1943-555X.0000464, doi:10.1061/(ASCE)IS.1943-555X.0000464.

15. Dorafshan, S., et al. *Unmanned Aerial Vehicle Augmented Bridge Inspection Feasibility Study.* Report No: CAIT-UTC-NC31, 2017.

16. Darby, Paul, William Hollerman, and John Miller. "Exploring the Potential Utility of Unmanned Aerial Vehicles for Practical Bridge Inspection in Louisiana." *MATEC Web of Conferences*, vol. 271, 2019, pp. 1001. *CrossRef*, https://search.proquest.com/docview/2276952051, doi:10.1051/matecconf/201927101001.

17. Tomiczek, Andrew P., et al. "Bridge Inspections with Small Unmanned Aircraft Systems: Case Studies." *Journal of Bridge Engineering*, vol. 24, no. 3, 2019, pp. 5019003. *CrossRef*, http://ascelibrary.org/doi/abs/10.1061/(ASCE)BE.1943-5592.0001376, doi:10.1061/(ASCE)BE.1943-5592.0001376.

18. Seo, Junwon, Luis Duque, and Jim Wacker. "Drone-Enabled Bridge Inspection Methodology and Application." *Automation in Construction*, vol. 94, 2018, pp. 112-126. *CrossRef*, https://dx.doi.org/10.1016/j.autcon.2018.06.006, doi:10.1016/j.autcon.2018.06.006.

19. Liu, Yu-Fei, et al. "Image-based Crack Assessment of Bridge Piers using Unmanned Aerial Vehicles and Three-dimensional Scene Reconstruction." *Computer-Aided Civil and Infrastructure Engineering*, vol. 35, no. 5, 2020, pp. 511-529. *CrossRef*, https://onlinelibrary.wiley.com/doi/abs/10.1111/mice.12501, doi:10.1111/mice.12501.

20. Bolourian, Neshat, and Amin Hammad. "LiDAR-Equipped UAV Path Planning Considering Potential Locations of Defects for Bridge Inspection." *Automation in Construction*, vol. 117, 2020, pp. 103250. *CrossRef*, https://dx.doi.org/10.1016/j.autcon.2020.103250, doi:10.1016/j.autcon.2020.103250.

21. Omar, Tarek, and Moncef L. Nehdi. "Remote Sensing of Concrete Bridge Decks using Unmanned Aerial Vehicle Infrared Thermography." *Automation in Construction*, vol. 83, 2017, pp. 360-371. *CrossRef*, https://dx.doi.org/10.1016/j.autcon.2017.06.024, doi:10.1016/j.autcon.2017.06.024..

22. Salaan, Carl J. O., et al. "Close Visual Bridge Inspection using a UAV with a Passive Rotating Spherical Shell." *Journal of Field Robotics*, vol. 35, no. 6, 2018, pp. 850-867. *CrossRef*, https://onlinelibrary.wiley.com/doi/abs/10.1002/rob.21781, doi:10.1002/rob.21781.

23. Kucuksubasi, Fatih, and Arzu Sorguc. "Transfer Learning-Based Crack Detection by Autonomous UAVs.", 2018, https://arxiv.org/abs/1807.11785.

24. Popescu, Cosmin, et al. "3D Reconstruction of Existing Concrete Bridges using Optical Methods." *Structure and Infrastructure Engineering*, vol. 15, no. 7, 2019, pp. 912-924. *CrossRef*, http://www.tandfonline.com/doi/abs/10.1080/15732479.2019.1594315, doi:10.1080/15732479.2019.1594315.

25. Tscharf, A., et al. "On the use of Uavs in Mining and Archaeology - Geo-Accurate 3d Reconstructions using various Platforms and Terrestrial Views." *ISPRS Annals of the Photogrammetry, Remote Sensing and Spatial Information Sciences*, vol. II-1/W1, no. 1, 2015, pp. 15-22. *CrossRef*, https://search.proquest.com/docview/1757018892, doi:10.5194/isprsannals-II-1-W1-15-2015.

26. Isailović, Dušan, et al. "Bridge Damage: Detection, IFC-Based Semantic Enrichment and Visualization." *Automation in Construction*, vol. 112, 2020, pp. 103088. *CrossRef*, https://dx.doi.org/10.1016/j.autcon.2020.103088, doi:10.1016/j.autcon.2020.103088.

27. Xu, Yiye, and Yelda Turkan. "BrIM and UAS for Bridge Inspections and Management." *Engineering, Construction, and Architectural Management*, vol. 27, no. 3, 2019, pp. 785-807. *CrossRef*, https://www.emerald.com/insight/content/doi/10.1108/ECAM-12-2018-0556/full/html, doi:10.1108/ECAM-12-2018-0556.

28. Inzerillo, Laura, Gaetano Di Mino, and Ronald Roberts. "Image-Based 3D Reconstruction using Traditional and UAV Datasets for Analysis of Road Pavement Distress." *Automation in Construction*, vol. 96, 2018, pp. 457-469. *CrossRef*, https://dx.doi.org/10.1016/j.autcon.2018.10.010, doi:10.1016/j.autcon.2018.10.010.

29. Bentley. *ContextCapture Guide for Photo Aquisition.* , 2017.

30. Zhong, Xingu, et al. "Assessment of the Feasibility of Detecting Concrete Cracks in Images Acquired by Unmanned Aerial Vehicles." *Automation in Construction*, vol. 89, 2018, pp. 49-57. *CrossRef*, https://dx.doi.org/10.1016/j.autcon.2018.01.005, doi:10.1016/j.autcon.2018.01.005.

31. Lei, Bin, et al. "New Crack Detection Method for Bridge Inspection using UAV Incorporating Image Processing." *Journal of Aerospace Engineering*, vol. 31, no. 5, 2018, pp. 4018058. *CrossRef*, http://ascelibrary.org/doi/abs/10.1061/(ASCE)AS.1943-5525.0000879, doi:10.1061/(ASCE)AS.1943-5525.0000879.

32. Peng, Xiong, et al. "The Feasibility Assessment Study of Bridge Crack Width Recognition in Images Based on Special Inspection UAV." *Advances in Civil Engineering*, vol. 2020, 2020. *Publicly Available Content Database*, https://dx.doi.org/10.1155/2020/8811649, doi:10.1155/2020/8811649.

33. Jeong, Euiseok, Junwon Seo, and James Wacker. "Literature Review and Technical Survey on Bridge Inspection using Unmanned Aerial Vehicles." *Journal of Performance of Constructed Facilities*, vol. 34, no. 6, 2020, pp. 4020113. *CrossRef*, http://ascelibrary.org/doi/abs/10.1061/(ASCE)CF.1943-5509.0001519, doi:10.1061/(ASCE)CF.1943-5509.0001519..

34. Dorafshan, Sattar, Robert J. Thomas, and Marc Maguire. "Fatigue Crack Detection using Unmanned Aerial Systems in Fracture Critical Inspection of Steel Bridges." *Journal of Bridge Engineering*, vol. 23, no. 10, 2018, pp. 4018078. *CrossRef*, http://ascelibrary.org/doi/abs/10.1061/(ASCE)BE.1943-5592.0001291, doi:10.1061/(ASCE)BE.1943-5592.0001291.

35. Chen, Qingcheng, et al. "Corrosion Detection for Large Steel Structure Base on UAV Integrated with Image Processing System." *IOP Conference Series. Materials Science and Engineering*, vol. 608, no. 1, 2019, pp. 12020. *CrossRef*, https://iopscience.iop.org/article/10.1088/1757-899X/608/1/012020, doi:10.1088/1757-899X/608/1/012020.

36. Sankarasrinivasan, S., et al. "Health Monitoring of Civil Structures with Integrated UAV and Image Processing System." *Procedia Computer Science*, vol. 54, 2015, pp. 508-515. *CrossRef*, https://dx.doi.org/10.1016/j.procs.2015.06.058, doi:10.1016/j.procs.2015.06.058.

37. Kim, H., S. H. Sim, and S. Cho. "Unmanned Aerial Vehicle (UAV)-Powered Concrete Crack Detection
Based on Digital Image Processing
." *6th International Conference on Advances in Experimental Structural Engineering*, 2015.

38. Gopalakrishnan, K., et al. "Crack Damage Detection in Unmanned Aerial Vehicle Images of Civil Infrastructure using Pre-Trained Deep Learning Model." *International Journal for Traffic and Transport Engineering*, vol. 8, no. 1, 2018, pp. 1-14. *CrossRef*, doi:10.7708/ijtte.2018.8(1).01.

39. Li, Yundong, Antonios Kontsos, and Ivan Bartoli. "Automated Rust-Defect Detection of a Steel Bridge using Aerial Multispectral Imagery." *Journal of Infrastructure Systems*, vol. 25, no. 2, 2019, pp. 4019014. *CrossRef*, http://ascelibrary.org/doi/abs/10.1061/(ASCE)IS.1943-555X.0000488, doi:10.1061/(ASCE)IS.1943-555X.0000488.

40. Saleem, Muhammad R., et al. "Instant Bridge Visual Inspection using an Unmanned Aerial Vehicle by Image Capturing and Geo-Tagging System and Deep Convolutional Neural Network." *Structural Health Monitoring*, vol. 20, no. 4, 2021, pp. 1760-1777. *CrossRef*, https://journals.sagepub.com/doi/full/10.1177/1475921720932384, doi:10.1177/1475921720932384.

41. Federal Highway Administration. *Design Example 1: Three-Span Continuous Straight Composite Steel I-Girder Bridge* . , 2015.

42. Erdelj, Milan, et al. "UAVs that Fly Forever: Uninterrupted Structural Inspection through Automatic UAV Replacement." *Ad Hoc Networks*, vol. 94, 2019, pp. 101612. *CrossRef*, https://dx.doi.org/10.1016/j.adhoc.2017.11.012, doi:10.1016/j.adhoc.2017.11.012.

43. DJI. "PHANTOM 4 PRO Specs.", https://www.dji.com/phantom-4-pro/info#specs.

44. ANSYS. "Static Structural Analysis.", 2019, https://ansyshelp.ansys.com/account/secured?returnurl=/Views/Secured/corp/v195/wb_sim/ds_static_mechanical_analysis_type.html.

45. ANSYS. *Chapter 4: Static Structural Analysis.* , 2009.

46. Stratasys. "VeroClear.", https://www.stratasys.com/materials/search/veroclear.

47. Stratasys. *PolyJet Materials Data Sheet.*

48. McMaster-Carr. "Epoxy Structural Adhesives for Harsh Environments.", https://www.mcmaster.com/adhesives/structural-adhesives/epoxy-structural-adhesives-for-harsh-environments/.

49. LOCTITE. *Loctite® Ea E-120hp.* , 2020.

# 8. VITA

Nalin Naranjo is a graduate student in the College of Engineering at the University of Illinois at Chicago where she also received her Bachelor of Science in Civil Engineering in 2020. She will earn a Master of Science in Civil Engineering from the University of Illinois at Chicago in 2021.